Universität Hamburg

Silicon Photomultipliers: Properties and Application in a Highly Granular Calorimeter

Nils Feege

Diplomarbeit

Institut für Experimentalphysik
Universität Hamburg
Oktober 2008

Abstract

Silicon Photomultipliers (SiPMs) are novel semiconductor-based photodetectors operated in Geiger mode. Their response is not linear, and both their gain and their photon detection efficiency depend on the applied bias voltage and on temperature.
The CALICE collaboration investigates several technology options for highly granular calorimeters for the future ILC. The prototype of a scintillator-steel sampling calorimeter with analogue readout for hadrons constructed at DESY and successfully operated in testbeam experiments at DESY, CERN and FNAL by this collaboration is the first large scale application for 7608 SiPMs developed by MEPhI.
This thesis deals with properties of the SiPMs used in the calorimeter prototype. The effective number of pixels of the SiPMs, which influences their saturation behaviour, is extracted from in situ measurements and compared to results obtained for the bare SiPMs. In addition, the effects of temperature and voltage changes on the parameters necessary for the calibration of the SiPMs and the detector are determined. Methods which allow for correcting or compensating these effects are evaluated. An approach to improve the absolute calibration of the temperature sensors in the prototype is described and temperature profiles are studied. Finally, a procedure to adjust the light yield of the cells of the prototype is presented. The results of the application of this procedure during the commissioning of the detector at FNAL are discussed.

Zusammenfassung

Silizium Photonenverfielfacher (SiPMs) sind neuartige halbleiterbasierte Photodetektoren, die im Geiger-Modus betrieben werden. Ihr Ansprechverhalten ist nicht linear, und sowohl ihr Verstärkungsfaktor als auch ihre Nachweiseffizienz für Photonen sind abhängig von angelegter Betriebsspannung und Temperatur.
Die CALICE Kollaboration erforscht mehrere Technologieoptionen für hochauflösende Kalorimeter für den zukünftigen ILC. Der von dieser Kollaboration am DESY konstruierte und erfolgreich in Testrahlexperimenten am DESY, am CERN und am FNAL betriebene Prototyp eines Szintillator-Stahl-Samplingkalorimeters mit analoger Auslese für Hadronen ist die erste Großanwendung für 7608 vom MEPhI entwickelte SiPMs.
Diese Arbeit befasst sich mit Eigenschaften der im Kalorimeterprototypen verwendeten SiPMs. Die effektive Pixelzahl der SiPMs, die ihr Sättigungsverhalten bestimmt, wird aus in situ Messungen gewonnen und mit Ergebnissen für die bloßen SiPMs verglichen. Außerdem werden die Einflüsse von Temperatur- und Spannungsänderungen auf die für die Kalibration der SiPMs und des Detektors benötigten Größen bestimmt. Es werden Methoden erprobt, die es ermöglichen, diese Einflüsse zu korrigieren oder zu kompensieren. Eine Vorgehensweise zur Verbesserung der absoluten Kalibration der Temperatursensoren im Prototype wird beschrieben und Temperaturprofile werden untersucht. Schließlich wird ein Verfahren zur Anpassung der Lichtausbeute der Zellen des Prototypen vorgestellt. Die Ergebnisse der Anwendung dieses Verfahrens während der Inbetriebnahme des Detektors am FNAL werden erörtert.

Contents

Introduction

In the past decades, high energy physics has made great progress in uncovering the constituents of matter and the forces between them. A model has evolved from the close interplay between advancing theories and experimental techniques. Today, this model is called the Standard Model of particle physics. The Standard Model includes 12 fermions: 6 quarks and 6 leptons. All matter we see is assembled from these elementary particles, according to well understood directions. In addition, the Standard Model gives an explanation for all observed forces, except for gravity: electromagnetism interacting between charged particles, the weak force interacting between all fermions and the strong force interacting between quarks. The forces are mediated via vector bosons. All fermions and vector bosons have been created and detected in experiments, and all experimental data agree with the Standard Model very well.

Despite this enormous success, the Standard Model still misses one important fragment. The question of how the particles acquire their masses has not been utterly solved yet. The Standard Model offers the so-called Higgs mechanism as an answer, but this mechanism postulates an additional particle, the Higgs boson, with a mass in a certain range. Until now, no experiment has succeeded in finding this particle.

A new generation of accelerator experiments aims for finally confirming or excluding the existence of the Standard Model Higgs boson. These experiments will explore uncharted energy ranges, where they may encounter Supersymmetry, extra dimensions or other physics beyond the Standard Model. The first accelerator capable of accessing these new energies is the Large Hadron Collider (LHC) at CERN[1], which has started its operation this year. A planned future project is the International Linear Collider (ILC), which is a high precision machine complementary to the LHC.

The ILC Reference Design Report [3] published in 2007 defines the accelerator outline based on superconducting cavities, different detector concepts and several technology options for the single detector components. The jet energy resolution demanded for ILC detectors can be achieved by applying Particle Flow reconstruction algorithms. This approach requires a high spatial resolution of both the tracking system and the calorimeters.

The CALICE collaboration investigates fine segmented calorimeters suited for Particle Flow algorithms. In the context of these investigations, the physics prototype of an analogue scintillator-steel sampling calorimeter for hadrons (AHCAL) has been constructed

[1] Conseil Européenne pour la Recherche Nucléaire, Geneva, Switzerland

at DESY[2] and successfully operated during testbeam experiments at DESY, CERN and FNAL[3]. This prototype is the first large scale application for Silicon Photomultipliers (SiPMs), which are photodetectors operated in Geiger mode developed by MEPhI[4]. Each of the scintillator tiles in the prototype is read out by an individual SiPM. Calibration and performance of photodetectors in Geiger mode change with operation conditions. The corresponding dependencies have to be understood and quantified, so that corrections for or compensations of these effects are possible.

The first chapter of this thesis gives an introduction to Particle Flow reconstruction algorithms and an overview of the International Large Detector (ILD), which is one of the ILC detector concepts optimised for the application of Particle Flow algorithms. Different technology options for the calorimeters of the ILD are briefly summarised. Afterwards, basic principles of calorimetry in particle physics experiments are explained.

In chapter two, the general layout and working principle of semiconductor-based photodetectors operated in Geiger mode are illustrated. The gain, the photon detection efficiency and the total response of these devices are discussed, as well as the dependence of these parameters on the operation voltage and on temperature. In addition, the saturation of the response signal with increasing intensity of the incident light is explained.

Chapter three describes the AHCAL physics prototype, its LED based calibration and monitoring system and the readout chain. The calibration procedure converting recorded ADC channels to measured energy depositions in the detector cells and all parameters needed for this are explained. Furthermore, properties of the SiPM sample used in the AHCAL physics prototype are quoted.

In chapter four, the effective number of pixels of the SiPMs in the AHCAL physics prototype is determined from in situ measurements and compared to the values obtained for the bare SiPMs. In addition, the bias voltage and temperature dependencies of the gain and the response of these SiPMs are investigated using calibration data collected at DESY and during the testbeam periods at CERN and FNAL.

The calibration of the temperature sensors in the prototype is explained in chapter five. Methods to correct for temperature changes and to predict the effects of bias voltage shifts are tested. The uncertainties introduced by these methods are evaluated. Finally, a procedure to scale the light yield of the cells of the AHCAL physics prototype via voltage adjustment is presented. The light yield is a measure of the detector performance. Results from this chapter have been successfully applied during the commissioning of the detector at the beginning of the first FNAL testbeam period.

[2]Deutsches Elektronen SYnchrotron, Hamburg, Germany
[3]Fermi National Accelerator Laboratory, Batavia, IL, USA
[4]Moscow Engineering and Physics Institute, Moscow, Russia

Chapter 1

A Calorimeter for the ILC

1.1 The International Linear Collider

In the near future, experiments at the Large Hadron Collider (LHC) at CERN will provide first insights into physics at the Terascale. The LHC is a proton ring collider operating at a centre of mass energy of up to $\sqrt{s} = 14\,\text{TeV}$. This energy scope allows for the generation of new particles in a totally unexplored mass region. If there is a Higgs boson, the LHC will most probably discover it. If supersymmetric particles exist, some of them will most likely be spotted at the LHC as well. The list of possible discoveries is long, the list of unexpected discoveries may be even longer.

Despite the great physics potential of the LHC, there are some drawbacks. The colliding protons are compound objects containing quarks and gluons. Each of these constituents, which are the actual collision partners, carries only a fraction of the proton momentum. As a result, the initial states of the scattering processes are not accurately known. In addition, the nature of the strong force leads to a large bulk of background events accompanying each "interesting" event and an enormous radiation exposure of the detectors. All this makes precision measurements of parameters like spin or parity extremely difficult.

The planned International Linear Collider (ILC) is a project complementary to the LHC [3]. At the ILC, electrons and positrons collide at centre of mass energies of up to $\sqrt{s} = 500\,\text{GeV}$. An upgrade to $\sqrt{s} = 1\,\text{TeV}$ is possible. According to present knowledge, electrons and positrons are elementary particles without substructure. Their interactions in a collider experiment have well known initial states and expose the detectors to only low radiation. Thus, the ILC offers the possibility to do high precision measurements in a much cleaner and better determined environment than given at the LHC.

To fully exploit the potential of a high precision machine like the ILC, new detectors of unprecedented performance are required. The expected ILC physics programme is dominated by multi-boson processes resulting in final states containing many jets. The intended physics analyses demand a clear separation of jets originating from W and Z boson decays. Only detectors with a jet energy resolution of at least $\frac{30\,\%}{\sqrt{E}}$ can make this distinction.

One approach which is expected to meet this resolution requirement is the application of Particle Flow reconstruction algorithms. The idea of Particle Flow is briefly described in section 1.1.1. The International Large Detector concept (ILD) is one of the ILC detector concepts which are optimised for the application of these reconstruction algorithms [4]. It is based on two previous layouts, the Large Detector Concept (LDC) and the Global Large Detector (GLD) [3]. Section 1.1.2 gives a brief overview over the basic ILD design. Various technology options for the different detector components are investigated.

1.1.1 Particle Flow

Common particle physics detectors comprise a tracking device, an electromagnetic calorimeter (ECAL) and a hadronic calorimeter (HCAL). For high relativistic particles, the momentum information obtained by the tracker corresponds to an energy determination. Thus, all three components can be used to measure the energies of charged particles. At most energies, the tracker provides the best energy resolution and is preferred. However, neutral particles and photons traverse the tracker without leaving a trace. Their energies can only be measured in the calorimeters.

On average, charged particles account for 65 % of the energy of a jet. Photons contribute 26 %, and neutral hadrons make up the remaining 9 % [5]. The idea of Particle Flow is to use the energy measurements from the best suited detector component for each particle type in a jet. Energies of charged particles are obtained from the tracker, photon energies from the ECAL and the energies of neutral hadrons from the HCAL. This method requires that each individual particle and photon inside a jet is reconstructed. In addition, showers in the calorimeters have to be assigned to the correct origins and signals from close showers have to be isolated properly. A strong magnetic field separating neutral from charged jet components, a tracking system with a high detection efficiency for charged particles and highly granular calorimeters are needed to meet these demands.

The jet energy resolution σ_{jet} achieved by Particle Flow [5] depends on the individual energy measurement resolutions for charged particles ($\sigma_{h^\pm}$), photons (σ_γ) and neutral hadrons (σ_{h^0}):

$$\sigma^2_{jet} = \sigma^2_{h^\pm} + \sigma^2_\gamma + \sigma^2_{h^0} + \sigma^2_{confusion} + \sigma^2_{threshold} + \sigma^2_{losses} \,. \tag{1.1}$$

The additional terms take into account wrong assignment of showers, or shower parts, to charged or neutral particles ($\sigma_{confusion}$), particles that are not reconstructed (σ_{losses}) and effects of the threshold energy ($\sigma_{threshold}$), which is the minimum energy a signal must have not to be rejected. Detector optimisation for Particle Flow performance aims for minimising both the contribution from confusion and the loss of particles in the detector.

1.1.2 The International Large Detector

The International Large Detector (ILD) bases on the Large Detector Concept (LDC) and the Global Large Detector (GLD). An image of the LDC detector simulated with MOKKA

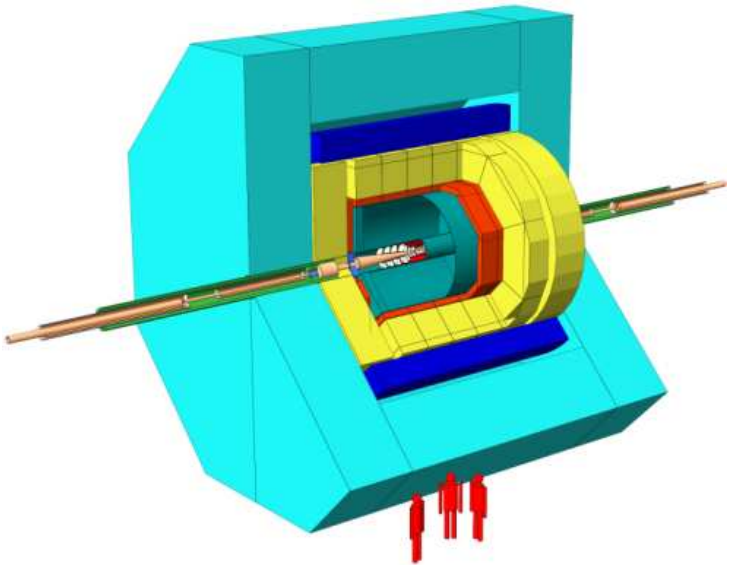

Figure 1.1: View of the LDC detector concept, as simulated with the MOKKA simulation package [3].

is displayed in figure 1.1 to exemplify the basic design of these detectors. The following overview of the single detector components is valid for LDC, as well as for GLD and ILD.

The detector part closest to the interaction point is a multilayer Silicon pixel vertex detector, which provides a high spatial resolution. This vertex detector is surrounded by a large Time Projection Chamber (TPC), which is the main tracking device. Discs of Silicon pixel and strip detectors in the forward regions make tracking down to small polar angles possible.

The TPC is enclosed by an electromagnetic calorimeter (ECAL), followed by a hadronic calorimeter (HCAL). Both ECAL and HCAL are sampling calorimeters, i.e. layers of sensitive material are separated by layers of absorber material. Sampling calorimeters and some basic concepts of calorimetry are explained in section 1.2. The absorber layers of the ECAL are made of tungsten, those of the HCAL are made of steel. For the sensitive layers of ECAL and HCAL, plastic scintillator stripes or tiles with analogue readout via photodetectors operated in Geiger mode are under investigation. This type of photodetectors is explained in chapter 2. The CAlorimeter for the LInear Collider with Electrons (CALICE) collaboration [6] has constructed a physics prototype of the analogue HCAL, which is described in chapter 3. Other HCAL designs use Gas Electron Multiplier foils, Micromegas or Resistive Plate Chambers for digitally read-out sensitive layers, while an alternative ECAL design uses Silicon detectors as active layers. Small calorimeters placed in the forward regions measure luminosity and other beam and collision parameters.

The ECAL and the HCAL are surrounded by a superconducting coil. The coil creates a longitudinal magnetic field of several tesla strength inside the detector. This field bends the tracks of charged particles, and from the curvature the particle momenta can be measured.

The outermost detector component is an iron return yoke for the magnetic flux. Gaps in the return yoke are instrumented to hold a muon detection system.

1.2 Calorimetry in Particle Physics

Particles and photons traversing matter lose energy due to several interaction processes. The relative contribution of the different processes to the overall energy loss depends strongly on the particle type, the energy and on the material the particle interacts with. Charged leptons and photons interact only electromagnetically, while neutral hadrons are only subject to the strong force. Charged hadrons lose energy both via electromagnetic and via strong processes. Some of these interactions generate new particles or photons, which again interact. This multiplication may repeat several times and is called, depending to the initial particle, an electromagnetic or hadronic shower. In general, a calorimeter measures the energy deposited in matter by an incident particle, aiming for reconstructing the initial energy of this particle.

1.2.1 Interactions of Charged Particles with Matter

Charged particles of moderate energies ($\beta\gamma \approx 0.1 - 1000$) other than electrons or positrons mainly lose energy by exciting or ionising the atoms of the material they pass through, i.e. they transfer energy to electrons bound to atomic nuclei and either raise them to higher energetic states or free them. The Bethe-Bloch equation [8] yields the mean energy $\mathrm{d}E$ per path length $\mathrm{d}x$ a particle of charge ze deposits in an absorber of atomic number Z and atomic mass A via ionisation processes:

$$-\frac{\mathrm{d}E}{\mathrm{d}x} = Kz^2\frac{Z}{A}\frac{1}{\beta^2}\left(\frac{1}{2}\ln\frac{2m_e c^2\beta^2\gamma^2 T_{max}}{I^2} - \beta^2 - \frac{\delta(\beta\gamma)}{2}\right) . \tag{1.2}$$

A maximum energy of T_{max} can be transfered to an electron of the absorber material in a single collision. The parameter I is the mean excitation energy, and K substitutes for a constant term including Avogadro's number, the elementary charge e and the electron mass m_e. At relativistic energies, the electric field of a charged particle flattens and extends until it is screened by polarisation of the absorber atoms. This density effect is taken into account by the function $\delta(\beta\gamma)$.

Figure 1.2 displays $-\frac{\mathrm{d}E}{\mathrm{d}x}$ according to equation 1.2 for positive muons (μ^+) in copper as a function of $\beta\gamma$. The energy deposition has a broad minimum around $\beta\gamma \approx 3-4$. Particles having energies in this range are called minimum ionising particles (MIPs). Below $\beta\gamma \approx 0.1$, some additional corrections need to be applied [8]. Above $\beta\gamma \approx 1000$, energy losses due to radiation processes become dominant.

Charged particles which are deflected inside the electric field of absorber atoms emit bremsstrahlung. This radiation always arises when a charged particle is accelerated inside an external electric field. The resulting energy loss of a particle with mass m and energy E

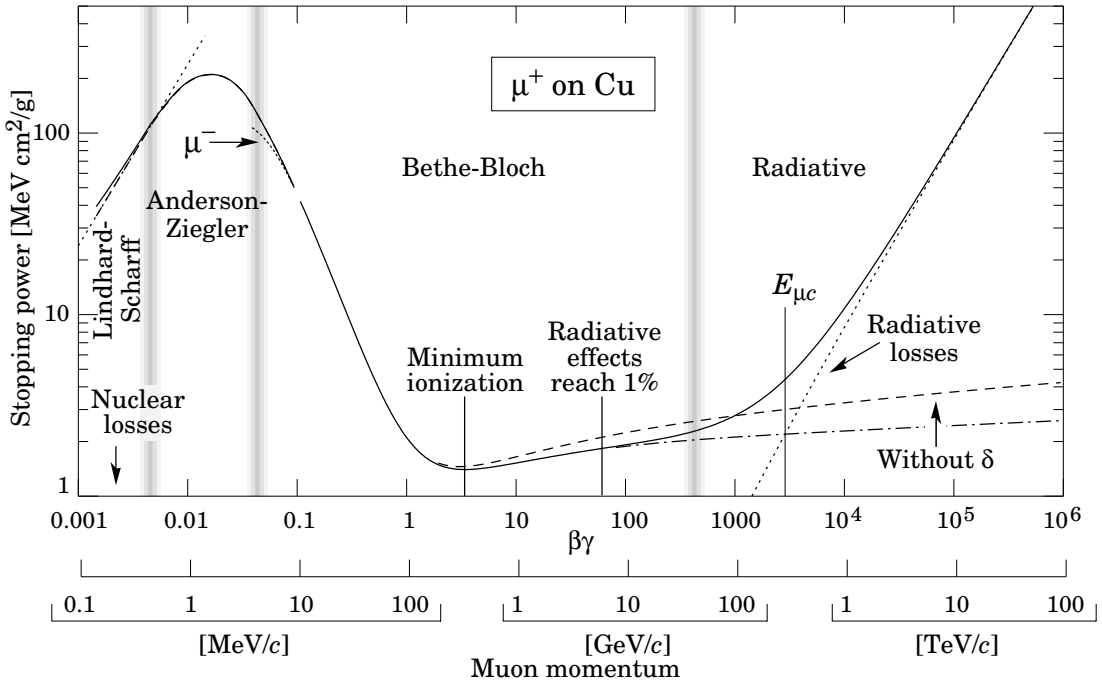

Figure 1.2: Energy loss of charged particles in matter [8]. For moderate energies, the dominant energy loss process (ionisation of absorber atoms) is described by equation 1.2.

is proportional to $\frac{E}{m^2}$. Thus, the emission of bremsstrahlung dominates the energy loss of electrons and positrons already at relatively low energies of less than $\approx 100\,\mathrm{MeV}$, while it contributes significantly to the energy loss of heavier particles only at much higher energies.

Another radiation process reducing a the energy of a charged particle is the emission of Čerenkov light. This light is emitted in a cone with opening angle θ_c to the movement direction of a particle if the velocity v of the particle in a dispersive medium of refractive index n is larger than the phase speed $\frac{c}{n}$ of light in this medium. The opening angle is given by

$$\cos\theta_c = \left(\frac{1}{n\beta}\right) \ . \tag{1.3}$$

The light emission is caused by polarisation of excited atoms along the path of the particle. Detecting Čerenkov light can be used to determine the energy of a particle, but since Čerenkov light consists of only few photons, the contribution of this process to the total energy loss of a particle is negligible.

There are two other ways charged particles can deposit energy in matter. A high energetic charged particle hitting an absorber electron can transfer an amount of energy much larger than the ionisation energy of the electrons, creating a so-called knock-on electron, or δ-ray. At very high energies, the electromagnetic interactions of charged particles with the atoms of the absorber material may cause nuclear reactions.

1.2.2 Interactions of Photons with Matter

Low energetic photons traversing matter are absorbed by atoms. The received energy can free an electron from its atomic boundary. This process is called the photoelectric effect. Another possible photon interaction at low energies is the Rayleigh scattering, which is the energy-loss free deflection of a photon by an atomic electron.

At higher energies, photons mainly lose energy due to Compton scattering on electrons bound to the absorber atoms. In this process, the photons transfer energy and momentum to the electrons and free them.

If the energy of a photon exceeds twice the electron rest mass, this photon may convert to an electron-positron ($e^- - e^+$) pair in the Coulomb field of a nucleus or in the field of atomic electrons. The latter process is only significant for high energetic photons in low-Z absorber materials.

1.2.3 Electromagnetic Showers

A high energetic charged particle passing through mater emits bremsstrahlung photons. If some of these photons have energies $> 2m_e$, they convert into electron-positron pairs, which again lose energy due to bremsstrahlung. A multiplication of particles and photons occurs. This cascade is called an electromagnetic shower. The shower spreads radially away from the direction of the incident particle. The multiplication continues until the generated bremsstrahlung photons do not have enough energy to convert to further electron-positron pairs. The following interactions with the absorber material decrease the number of shower particles and photons. An incident photon may initiate a shower like this as well.

The development of an electromagnetic shower can be described by the radiation length X_0 and the Molière radius ρ_M, which characterise the longitudinal and the transverse shower shapes independently from the absorber material. The radiation length X_0 is defined as the distance in the absorber over which electrons or positrons of energies $>>$ 1 GeV emit $(1 - e^{-1}) = 63.2\,\%$ of their initial energy as bremsstrahlung. The probability of a photon to interact while traversing $\frac{9}{7}X_0$ of absorber material is 63.2 %. This distance is called the mean free photon path. The Molière radius is the radius of a cylinder along the movement direction of an incident particle that contains 90 % of the energy deposited by an electromagnetic shower.

1.2.4 Hadronic Showers

Hadrons interact with traversed material via the strong force. Various processes are possible, during which the hit nucleus, the incident particle or both of them may change their identity and new hadrons can be generated. As for the electromagnetic showers, a particle multiplication occurs, which dies out after reaching a maximum. Although the average shape of hadronic and electromagnetic showers are very similar, hadronic showers are much broader and subject to large and hard to parametrise fluctuations. In addition,

a significant part of the energy of an incident hadron may be deposited as neutrons, neutrinos or excitation energy of atomic nuclei. These energy depositions are invisible to most calorimeter systems and increase the uncertainty of calorimetric energy measurements for hadrons. All charged hadrons lose part of their energy due to the electromagnetic processes described in section 1.2.1 as well.

The scale of hadronic showers is the nuclear interaction length λ_{int}, which is the mean distance a high energetic hadron passes through a medium before it interacts strongly with an atomic nucleus for the first time. The nuclear interaction length is considerably larger than the electromagnetic radiation length X_0. For iron, for example, $\frac{\lambda_{int}}{X_0}$ is about 9.5.

Hadronic showers contain electromagnetic showers. This electromagnetic fraction mainly originates from neutral pions (π^0) and etas (η) generated during strong processes. Each π^0 and η decays into two photons, each of which has enough energy to initiate an electromagnetic shower, as described in section 1.2.3.

1.2.5 Sampling Calorimeters

Calorimeters measuring energy depositions of particles can be designed in many different ways. One type which is often used in high energy physics experiments is the sampling calorimeter. Sampling calorimeters consist of several distinct layers of high density absorber material, like iron or uranium. The space between these passive layers is filled with a sensitive, or active, medium. Depending on the material used, the energy depositions of charged particles traversing the active medium generate either excited states, which deexcite via the emission of (scintillation) light, or free electrons. The light, or the electrons, are the basis of the energy deposition measurement. The sandwich structure allows for the use of the best suited absorber material, a cost reduction and a compact calorimeter design. In addition, sampling calorimeters yield the high longitudinal granularity required for the application of particle flow reconstruction algorithms. On the downside, the energy resolution of sampling calorimeters is often worse than the resolution of homogeneous calorimeters purely made of sensitive material, because the energy left in the passive layers cannot be detected.

There is no fundamental difference between calorimeters measuring the energies of particles of different types. Due do the larger expansion of hadronic showers compared to electromagnetic showers and due to the nuclear interaction length λ_{int}, which is wider than X_0, more or denser material is required to contain a certain fraction of a hadronic shower than to contain the same fraction of an electromagnetic shower.

1.2.6 Energy Resolution of a Calorimeter

The relative energy resolution $\frac{\sigma_E}{E}$ of a calorimeter is influenced by different parameters. First, the resolution depends on the statistical fluctuations of shower development. They follow Poisson distributions and scale with $\frac{1}{\sqrt{E}}$, i.e. they can be described by a term $\frac{a}{\sqrt{E}}$. For hadronic sampling calorimeters, the statistical fluctuations include variations of

the energy fraction deposited in the active material of the calorimeter and changes in the electromagnetic content from one hadronic shower to another. Second, the noise of a calorimeter needs to be taken into account. The relative noise contribution decreases with $\frac{1}{E}$ and can be written as $\frac{b}{E}$. Third, uncertainties in the detector calibration add a constant term c to the energy resolution. The total energy resolution is the quadratic sum of these three terms:

$$\frac{\sigma_E}{E} = \frac{a}{\sqrt{E}} \oplus \frac{b}{E} \oplus c = \sqrt{\left(\frac{a}{\sqrt{E}}\right)^2 + \left(\frac{b}{E}\right)^2 + c^2}\,. \tag{1.4}$$

Chapter 2

Semiconductor-based Photodetectors Operated in Geiger Mode

Photodetectors operated in Geiger mode are novel semiconductor devices applied for photon detection. Examples are the Silicon Photomultipliers (SiPMs) developed by the Moscow Engineering and Physics Institute (MEPhI) and Pulsar Enterprise [9, 10, 11] or the Multi-Pixel Photon Counters (MPPCs) designed by Hamamatsu [12, 13, 14]. These photodetectors are only a few mm^2 in size and insensitive to magnetic fields. In contrast to conventional photomultiplier tubes (PMTs), they can be used to measure light intensities directly inside experimental setups, even if magnetic fields are present or if there is only little space available. In addition, photodetectors in Geiger mode are operated at bias voltages of below 100 V. This value is small compared to the bias voltages of several kV required for PMTs, while the gain of both devices is of the same order of magnitude ($O(10^6)$). The working principle and properties of photodetectors in Geiger mode are explained in the following sections.

2.1 General Layout

Figure 2.1 (left) shows a picture of a Silicon Photomultiplier. Like all semiconductor-based photodetectors operated in Geiger mode, SiPMs consist of an array of single pixels. The depicted SiPM holds 34 x 34 pixels on an area of $1\,\mathrm{mm}^2$. Each pixel is a pn-diode operated in the so-called Geiger mode. Geiger mode operation means that a reverse bias voltage U_{bias} larger than the breakdown voltage U_{bd} of the pixel is applied. An electric field E of high intensity is created in the depletion region of the pn-junction. This is illustrated in figure 2.1 (right). Incident optical photons can be absorbed and generate electron hole pairs in the depletion region. The electric field in this region draws electrons and holes towards opposite ends of the pn-junction. Depending on the pixel material, this acceleration enables either the electrons, the holes or both of them to create additional free electrons and holes via impact ionisation. The additional free charge carriers are again accelerated until they

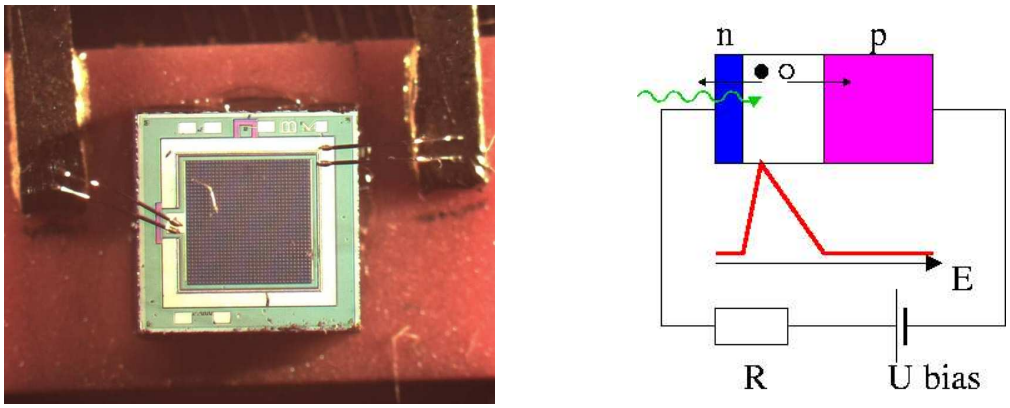

Figure 2.1: (left) Picture of a SiPM. The square centre part is the array of 34 x 34 pixels, the two outer stripes are electric contacts. (right) Schematic of a single pixel. A bias voltage U_{bias} is applied to a pn-junction via a quenching resistor R, creating a depletion region with a high electric field E. Incident optical photons can be absorbed and generate electron (closed dot) hole (open dot) pairs. Both charge carriers are accelerated to opposite sides of the pn-junction and can initiate Geiger discharges.

can ionise further atoms. An avalanche evolves. Due to the high electric field in Geiger mode, the avalanche sustains itself. This breakdown is called Geiger discharge, or "firing" of a pixel. Another feature of avalanches in Geiger mode is the independence of the number of created free charge carriers from the number of initially generated electron hole pairs. In other words, the output signal of a single pixel does not depend on the number of absorbed photons.

The self-sustaining behaviour, the high gain and the independence of the released charge from the number of initially generated electron hole pairs distinguishes Geiger discharges from avalanches in pn-junctions operated in avalanche mode. The Avalanche mode can be used for photon detection as well and is reached by applying bias voltages close to, but below breakdown voltage [15].

With the pixel design described so far, a once initiated Geiger discharge sustains itself for a long and hardly predictable time. Thus, a quenching resistor R is added to each pixel. When the pixel fires, the resulting current causes a voltage drop over the resistor. If the quenching resistor is chosen properly, the effective voltage at the pn-junction is reduced below the breakdown voltage and the avalanche dies out. The resistivity R_{quench} of the quenching resistor influences the time span between the initiation of a Geiger discharge and the complete recovery of the internal electric field, i.e. the moment the pixel can fire again. This recovery time τ can be calculated according to

$$\tau = R_{quench} \cdot C_{pix} \ . \tag{2.1}$$

C_{pix} is the single pixel capacitance. It is determined by the geometry of a pixel and the doping of the semiconductor material.

The gain of a photodetector in Geiger mode is defined as the number of electron hole pairs generated during the Geiger discharge of a single pixel. It is of the order 10^6. In the case of a SiPM, only the electron signal is read out. The ionisation coefficient in Silicon is significantly larger for electrons than for holes and only the electrons can initiate Geiger discharges [15]. In principle, the signal from the holes can be read out as well. A firing pixel releases a total charge

$$Q_{pix} = C_{pix} \cdot (U_{bias} - U_{bd}) \ , \tag{2.2}$$

which is equal to the gain multiplied with the elementary charge e [9].

Electron hole pairs generated in the depletion region of a pixel by thermal excitation can initiate Geiger discharges as well. This gives rise to noise, or dark current, of photodetectors in Geiger mode. Photons created during a Geiger discharge can migrate to an adjacent pixel and generate electron hole pairs there as well. The firing of additional pixels caused by this photon migration is called optical interpixel crosstalk.

2.2 Photon Detection Efficiency

The photon detection efficiency ε is the probability of a photon hitting a photodetector operated in Geiger mode to cause a Geiger discharge, i.e. the ratio between detected and incident photons. Measuring this efficiency requires a light source of known intensity to illuminate the photodetector. The photon detection efficiency is the product of the geometrical efficiency ε^{Geo}, the Quantum Efficiency ε^{QE} and the Geiger efficiency ε^{Geiger}. Geometrical efficiency is the ratio between the light sensitive area and the total surface of a photodetector. The Quantum Efficiency corresponds to the probability of a photon traversing the depletion region of a pixel to be absorbed and generate an electron hole pair. Geiger efficiency is the probability of a free electron or a hole in the depletion region of a pixel to initiate a Geiger discharge.

2.3 Response Signal and Saturation

The total response signal A of a photodetector operated in Geiger mode to incident light is a function of the number N_γ of photons hitting the device:

$$A(N_\gamma) = f_{pix}(N_\gamma \cdot \varepsilon \cdot (1 + \kappa)) \cdot G. \tag{2.3}$$

The parameter ε is the photon detection efficiency and κ is the optical interpixel crosstalk. Neglecting saturation effects, i.e. in a linear device, the expression $N_{ph.e.} = N_\gamma \cdot \varepsilon \cdot (1 + \kappa)$ corresponds to the number of firing pixels. The function $f_{pix}(N_{ph.e.})$, which gives the real number of firing pixels taking saturation into account, is discussed below. The gain G of the photodetector is the signal contribution of one firing pixel.

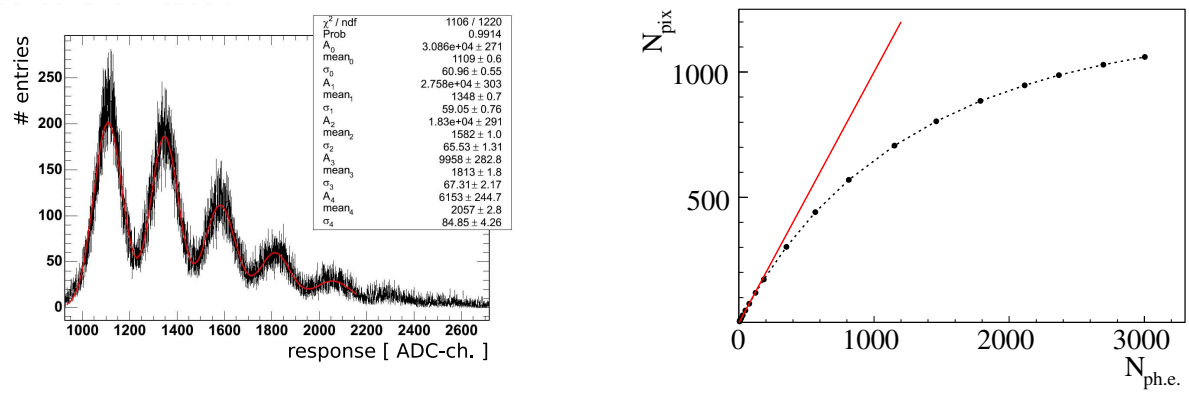

Figure 2.2: (left) Single pixel spectrum generated by illuminating a SiPM with pulsed low intensity (1-5 generated photoelectrons) LED light. The first peak is the pedestal, the second peak corresponds to one pixel firing, the third peak to two pixels firing and so on. The distance between the means of two peaks is a measure of the SiPM gain. (right) A SiPM response curve showing saturation. The number $N_{pix} = f_{pix}(N_{ph.e.})$ of firing pixels is plotted over $N_{ph.e.}$, which is proportional to the number N_γ of incident photons (closed dots). The solid line indicates the one to one correspondence between these numbers.

The response of a SiPM to pulsed LED light of low intensity (1-5 generated photoelectrons) is displayed in figure 2.2 (left). For intensities as low as this, $f_{pix}(N_{ph.e.})$ in equation 2.3 is the identity function, i.e. saturation effects are negligible. The first peak observed in figure 2.2 (left) is the pedestal, the second peak corresponds to one pixel firing, the third to two pixels firing and so on. The difference between the mean values of two peaks gives the SiPM gain G. Single pixel spectra like this can be used to determine the gain of any photodetector operated in Geiger mode.

The total number of pixels of a photodetector in Geiger mode is limited. If an electron hole pair is generated in a pixel that is recovering from a previous discharge, the pixel cannot fire again. The photoelectron and the hole do not contribute to the total response signal. Thus, the number of firing pixels and the response signal are subject to saturation effects. These effects become more dominant with increasing light intensity and are taken into account by the function $f_{pix}(N_{ph.e.})$ in equation 2.3. Figure 2.2 (right) shows the relation between $N_{ph.e.}$ and the number of actually firing pixels, $N_{pix} = f_{pix}(N_{ph.e.})$, for a SiPM. The solid line indicates the one to one correspondence between these values. The larger $N_{ph.e.}$ becomes, the more the observed relation deviates from linearity.

In first approximation, $f_{pix}(N_{ph.e.})$ is a single exponential function. Using this ansatz and equation 2.3, the response signal $A(N_\gamma)$ to incident light of the intensity N_γ is described by the function

$$A(N_\gamma) = N_{eff} \cdot (1 - \mathrm{e}^{-N_\gamma \cdot \frac{\varepsilon \cdot (1+\kappa)}{N_{eff}}}) \cdot G \,, \tag{2.4}$$

where N_{eff} is the effective number of pixels. This simple function does not describe the response curve well at all light intensities. Non-uniformities in the distribution of the

incident light lead to different probabilities for single groups of pixels to be hit by a photon. The light distribution can even vary with the light intensity. As a result, a sum of several exponential functions is needed to describe the SiPM response more accurately, one for each area of homogeneous illumination.

The saturation level, i.e. the maximum possible response signal of a photodetector operated in Geiger mode, is determined by the effective number of pixels N_{eff}. Assuming an infinite pixel recovery time τ and complete illumination, this number equals the number of physical pixels N_{phys}. In other words, if all pixels are fired, additional photons cannot increase the response signal further. However, since both τ and the pulse width of incident light are finite, a pixel may recover and fire several times during signal generation. As a result, the effective number of pixels may be larger than the number of physical pixels. On the other hand, if not all physical pixels are illuminated, N_{eff} can also be smaller than N_{phys}.

Equation 2.3 and 2.4 show that, in order to use any photodetector in Geiger mode for measuring light intensities, one needs to quantify the gain G, the photon detection efficiency ε and the interpixel crosstalk κ of the photodetector. In addition, the saturation behaviour and the effective number of pixels have to be known to make corrections for nonlinearity effects possible.

2.4 Voltage and Temperature Dependence of Operation Parameters

The gain G of a semiconductor-based photodetector depends on the difference between the applied bias voltage U_{bias} and the device specific breakdown voltage U_{bd}. Figure 2.3 shows the gain for constant breakdown voltage and varying bias voltage. As long as the bias voltage is considerably smaller than the breakdown voltage, the gain is 1. If U_{bias} approaches U_{bd}, the gain increases very quickly in a narrow voltage interval. This is the so-called avalanche region. As soon as U_{bias} passes U_{bd}, the device is in Geiger mode. From that point on, the gain increases only slightly and linearly with U_{bias}. Deriving equation 2.2 on page 13 and using $Q_{pix} = G \cdot e$ leads to the following relations for the absolute and the relative gain voltage dependencies, where $U = U_{bias}$:

$$\frac{\mathrm{d}G}{\mathrm{d}U} = \frac{C_{pix}}{e}\,, \tag{2.5}$$

$$\frac{1}{G}\frac{\mathrm{d}G}{\mathrm{d}U} = \frac{1}{(U_{bias} - U_{bd})}\,. \tag{2.6}$$

In Geiger mode, $\frac{\mathrm{d}G}{\mathrm{d}U}$ is a device-specific constant, which does not depend on the exact operation conditions. In contrast to this, $\frac{1}{G}\frac{\mathrm{d}G}{\mathrm{d}U}$ depends only on the difference between applied voltage and breakdown voltage and is independent from other characteristics of the device itself.

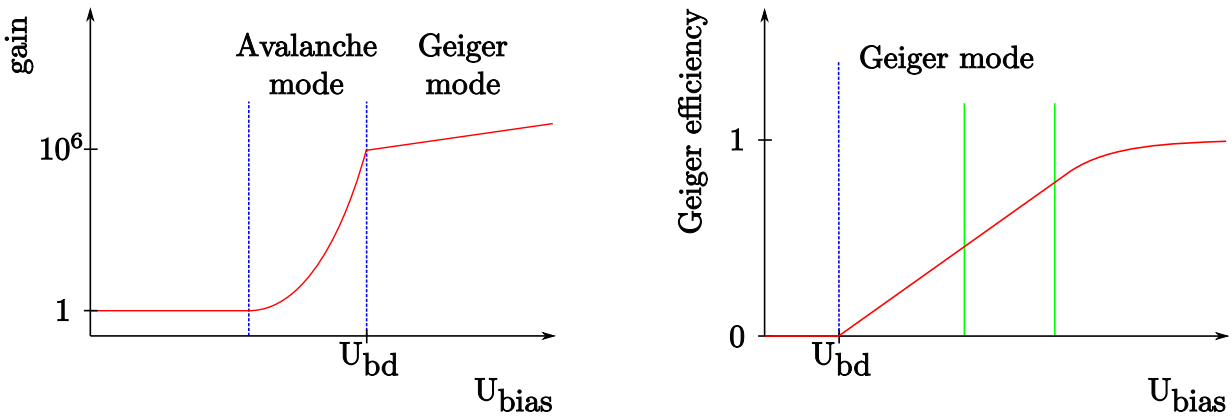

Figure 2.3: (left) Voltage dependence of the gain of a reverse-biased pn-junction used as a photodetector. As long as U_{bias} is considerably smaller than U_{bd}, the gain is 1. If U_{bias} comes close to U_{bd}, the gain increases rapidly. This is the avalanche region. For U_{bias} larger than U_{bd}, the gain depends only slightly and linearly on U_{bias}. This is the range of Geiger mode operation. (right) Voltage dependence of the Geiger efficiency ε^{Geiger}. Below Geiger mode, this efficiency is zero. In Geiger mode, it increases linearly with voltage until it saturates. The lines mark the area of common operation voltage for photodetectors in Geiger mode.

The Geiger efficiency ε^{Geiger}, and thus the total photon detection efficiency ε, depends on the difference $U_{bias} - U_{bd}$ as well. As illustrated in figure 2.3 (right), the Geiger efficiency is zero as long as the bias voltage is smaller than the breakdown voltage. In Geiger mode, ε^{Geiger} increases linearly with voltage until it saturates at 100 %. Usually, photodetectors in Geiger mode are operated at voltages below this saturation region.

The breakdown voltage U_{bd} of a Silicon pn-junction increases linearly with rising temperature T, as shown by measurements performed on MPPCs [16], for example. Figure 2.4 (left) displays the outcome of one of these measurements. For MPPC pixels, the breakdown voltage-temperature dependence $\frac{\mathrm{d}U_{bd}}{\mathrm{d}T}$ is $56.0 \pm 0.1 \frac{\mathrm{mV}}{\mathrm{K}}$ [17].

As a result of the relation between breakdown voltage and temperature, the difference $U_{bias} - U_{bd}$ and the gain of a photodetector in Geiger mode at a fixed U_{bias} are smaller for higher temperatures. Cooling down the photodetector increases the gain, accordingly. The relation between $\frac{\mathrm{d}G}{\mathrm{d}U}$ and $\frac{\mathrm{d}G}{\mathrm{d}T}$ is

$$\frac{\mathrm{d}G}{\mathrm{d}T} = \left(-\frac{\mathrm{d}U_{bd}}{\mathrm{d}T}\right) \cdot \frac{\mathrm{d}G}{\mathrm{d}U} \,. \tag{2.7}$$

Figure 2.4 (right) shows the gain at different bias voltages and at different temperatures for an MPPC. Qualitatively, the behaviour of a SiPM or another photodetector operated in Geiger mode is the same. The plot illustrates that a change in bias voltage at a fixed temperature corresponds to a certain temperature change at a fixed bias voltage. This feature can be used to compensate the effects of temperature variations on the gain by adjusting the bias voltage. Because of the different signs of the voltage and the temperature

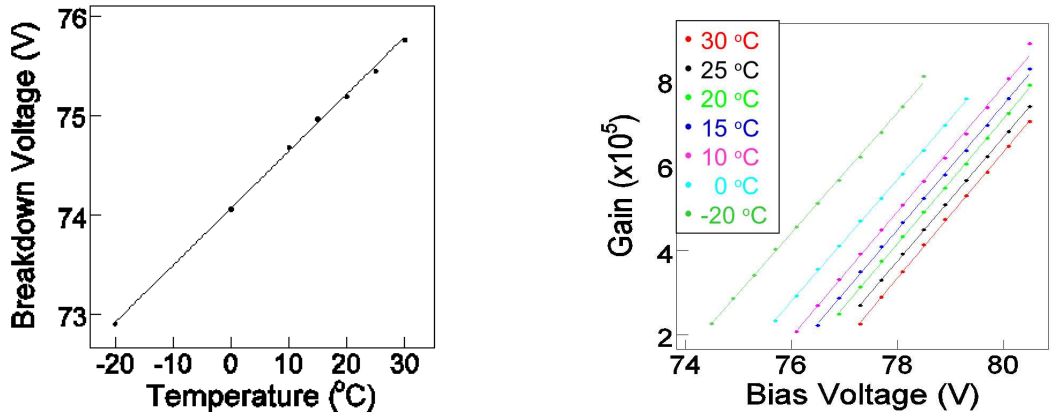

Figure 2.4: (left) Temperature dependence of the breakdown voltage of an MPPC pixel [16]. (right) Bias voltage dependence of the gain in Geiger mode at different temperatures for an MPPC [16]. Since the gain depends linearly on both voltage and temperature, changes in one parameter can compensate changes in the other.

dependence of the gain, the bias voltage needs to be increased to compensate temperature increases. However, this compensation amplifies the effects of temperature changes on the noise, since both a higher temperature and a higher bias voltage lead to an increase in the noise of a photodetector in Geiger mode.

The response A of a photodetector operated in Geiger mode is proportional to the product of G and ε. The relative voltage and temperature dependence of the response can be calculated according to

$$\frac{1}{A}\frac{\mathrm{d}A}{\mathrm{d}U} = \frac{1}{G}\frac{\mathrm{d}G}{\mathrm{d}U} + \frac{1}{\varepsilon}\frac{\mathrm{d}\varepsilon}{\mathrm{d}U} \tag{2.8}$$

and

$$\frac{1}{A}\frac{\mathrm{d}A}{\mathrm{d}T} = \frac{1}{G}\frac{\mathrm{d}G}{\mathrm{d}T} + \frac{1}{\varepsilon}\frac{\mathrm{d}\varepsilon}{\mathrm{d}T}\,. \tag{2.9}$$

The dependencies of both gain and photon detection efficiency on voltage or on temperature have the same sign. Thus, the dependencies of the response have higher absolute value than the respective dependencies of the gain.

As mentioned in the previous section, measuring light intensities with a photodetector operated in Geiger mode requires the prior determination of its gain, its photon detection efficiency and its saturation behaviour, including its effective number of pixels. Since the first two parameters depend on voltage and temperature, they must be given under the same voltage and temperature conditions under which the actual measurement is performed.

Chapter 3

The CALICE AHCAL Physics Prototype

The physics prototype of the Analogue Hadronic CALorimeter (AHCAL) built by the CAlorimeter for the LInear Collider with Electrons (CALICE) collaboration is a highly granular scintillator-steel sandwich calorimeter and a large scale application for Silicon Photomultipliers. Successful testbeam experiments with this prototype have been conducted at DESY, CERN and FNAL [19, 20].

The absorber structure of the AHCAL physics prototype consists of 1 x 1 m^2 large and 2 cm thick steel plates. These plates separate 38 active layers, or modules. The sensitive material of each layer is 0.5 cm thick. The total depth of the prototype is $\approx 4.5\ \lambda_{int}$ (see section 1.2.4).

The first 30 sensitive layers consist of 216 single plastic scintillator tiles, while the last 8 consist of only 141 tiles. The tile size varies between 3 x 3 cm^2, 6 x 6 cm^2 and 12 x 12 cm^2. A Silicon Photomultiplier (SiPM) is mounted on each tile, coupled via a wavelength-shifting fibre. This fibre collects the scintillation light and shifts it to green, where the SiPM is most sensitive. SiPMs are photodetectors operated in Geiger mode, which are described in chapter 2. The total number of SiPMs and tiles used for the prototype is 7608. An LED based system is used to calibrate the SiPMs and to monitor their operation parameters.

The high granularity in both longitudinal and transverse direction is needed to apply Particle Flow reconstruction algorithms, which are introduced in section 1.1.1. The prototype is used to help developing and testing these algorithms. In addition, it offers the possibility to study hadronic showers with a new level of resolution.

This chapter gives an overview of the AHCAL physics prototype, the modules, the signal generation, the readout chain, the calibration and monitoring system and the energy calibration procedure. Finally, properties of the SiPM sample used for the prototype are summarised. For more detailed information, see [21, 22, 19, 23].

3.1 Module Layout

The layout of an active layer, or module, of the AHCAL physics prototype is presented in figure 3.1. The centre part of each module is a metal cassette containing the plastic scintillator tiles, i.e. the sensitive material. The (i/j) coordinates specify the positions of the tiles within each layer. A Calibration and Monitoring Board (CMB) is connected to one side of this cassette. The CMBs are described in section 3.3. The opposite side of the cassette is connected to a second board, which contains the Very FrontEnd (VFE) electronics [24]. The VFE electronics is explained in section 3.2.

The first 30 modules of the AHCAL physics prototype house 216 plastic scintillator tiles. These modules have a fine inner core of 100 scintillator tiles of 3 x 3 cm^2 size, as indicated in figure 3.1. This inner core is surrounded by 96 tiles of 6 x 6 cm^2 size. Finally, there is an outer ring of 20 tiles of 12 x 12 cm^2 size. Modules 31 to 38 do not have the fine inner core, but 25 additional 6 x 6 cm^2 tiles instead. Thus, these coarse modules only comprise a total number of 141 tiles.

Figure 3.2 shows an exemplary 3 x 3 cm^2 scintillator tile. The organic material (BASF 130 from the Vladimir company) emits UV scintillation light with a wavelength peaked at 430 nm. A groove in each tile contains a wavelength-shifting fibre (Y11, 300 ppm from Kuraray). The fibre absorbs UV light and re-emits green light at wavelength of about 500 nm. A SiPM is coupled to one end of this fibre, a mirror covers the other end. Reflective foil (VN2000 superradiant from 3M) on the top and the bottom side of each tile and chemical treatment of the other tile sides minimise light losses and light crosstalk to neighbouring cells.

Each cassette of the AHCAL physics prototype modules comprises five temperature sensors. The positions of these sensors are indicated by the closed dots in figure 3.3. In modules 1 and 2, the temperature sensors are located along a diagonal axis from the top left to the bottom right, while the sensors in modules 3 to 38 are arranged from top to bottom. The sensors are numbered from 1 to 5. Both the CMBs and the VFE electronics boards contain two additional temperature sensors. The sensor positions are marked in figure 3.1 as well.

3.2 Signal Generation and Readout Chain

Energy deposited by a traversing particle in one of the scintillator tiles causes the generation of UV scintillation light. The wavelength-shifting fibre inside the tile collects this light, shifts it to green and guides it to the SiPM, which is coupled to one of its ends. The SiPM converts the incident light into an analogue electric signal. This signal is processed by an Application-Specific Integrated Circuit (ASIC) chip of the VFE electronics [22]. The ASICs are a development of the Laboratoire de l'Accél'erateur Lin'eaire (LAL) in France. Each of the 12 chips of the VFE electronics collects the signals from 18 SiPMs. After amplification and shaping, these signals are multiplexed to one output signal per chip and

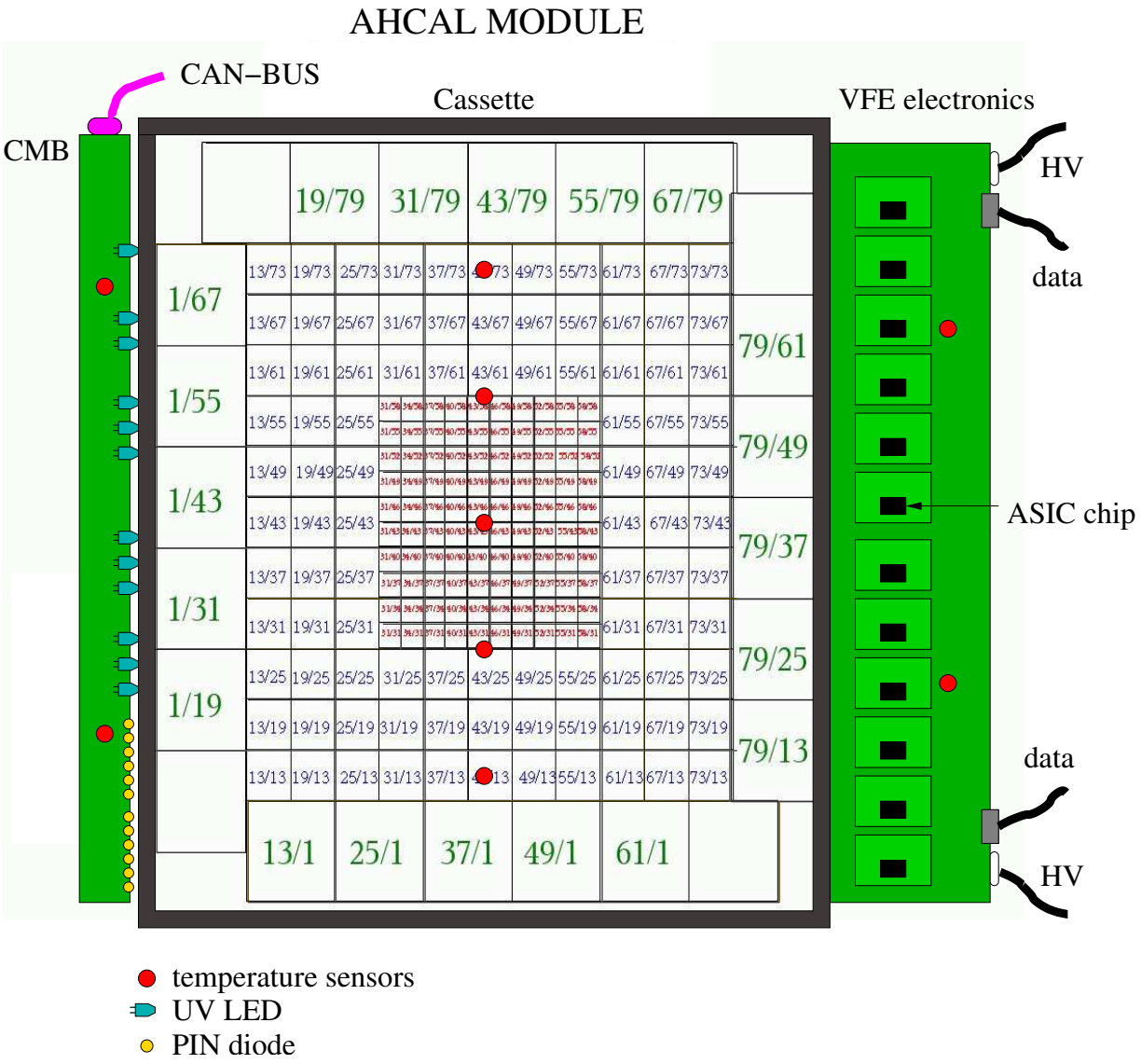

Figure 3.1: Layout of an AHCAL physics prototype module. The centre part is a 1 x 1 m^2 large metal cassette housing 216 (or 141) scintillator tiles. The (i/j) coordinates specify the tile positions within the cassette. Connected to the left side of the cassette is the Calibration and Monitoring Board (CMB), which contains 12 UV LEDs and 12 PIN diodes. Connected to the other side of the cassette is the Very Front End (VFE) electronics with the ASIC chips and connections to the external data acquisition system and the High Voltage (HV) power supplies. Each module has nine temperature sensors, five inside the cassette, two on the CMB and two on the VFE electronics board.

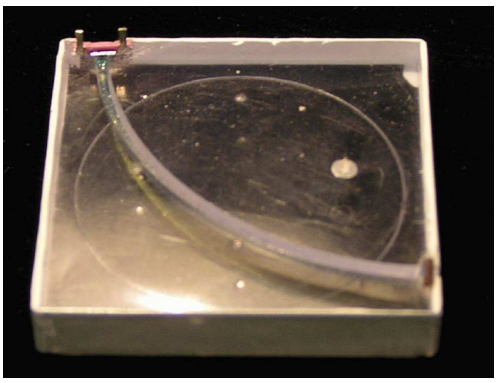

Figure 3.2: Plastic scintillator tile with a wavelength-shifting fibre and a SiPM, which is positioned in the top left corner of the tile. A mirror covers the lower right end of the fibre.

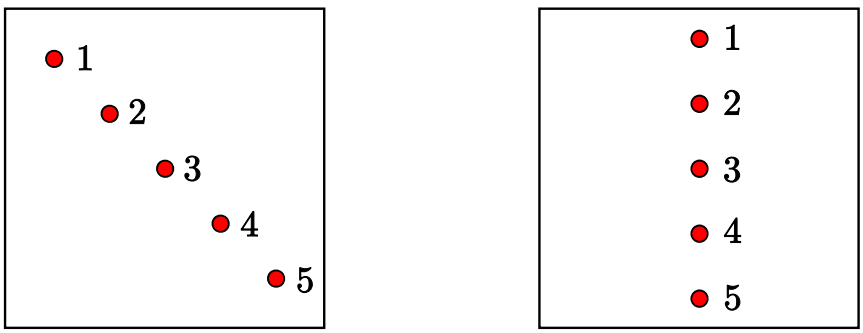

Figure 3.3: (left) Positions of the temperature sensors (closed dots) within the cassettes of modules 1 and 2. (right) Positions of the temperature sensors (closed dots) within the cassettes of modules 3 to 38.

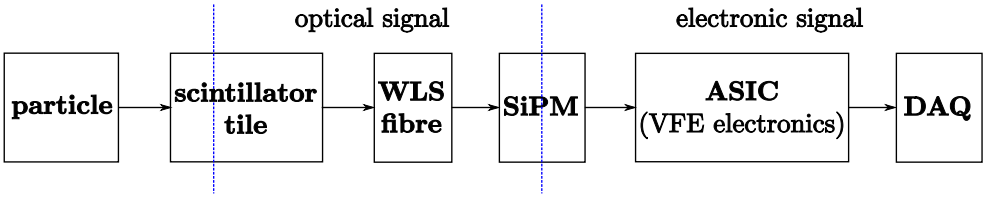

Figure 3.4: The readout chain: Scintillation light generated in a tile is collected by the WLS fibre, shifted to green and guided to a SiPM. The electronic SiPM output signal is processed by an ASIC of the VFE electronics and recorded by a DAQ system.

transfered to an external data acquisition system (DAQ). This readout chain is illustrated in figure 3.4.

The ASICs have two different operation modes. The physics mode (PM) is characterised by a gain of $G_{PM} = 8.18\,\frac{\mathrm{mV}}{\mathrm{pC}}$ and a shaping time of 150 ns. This mode is used for measuring energy depositions in the detector. The calibration mode (CM) has a gain of $G_{CM} = 92.3\,\frac{\mathrm{mV}}{\mathrm{pC}}$ and a shaping time of 40 ns. The high amplification of the calibration mode is needed to resolve single pixel spectra, which are used for the SiPM gain calibration (see section 3.3). Because of its lower gain, the physics mode offers a larger dynamic range than the calibration mode. The ratio between the two amplifications is the ASIC intercalibration factor

$$IC_{ASIC} = \frac{G_{PM}}{G_{CM}}\,. \tag{3.1}$$

The intercalibration factor of an AHCAL cell, IC_{cell}, is defined as

$$IC_{cell} = \frac{A_{PM}}{A_{CM}}\,, \tag{3.2}$$

where A_{PM} is a signal measured in physics mode and A_{CM} is the same signal measured in calibration mode. Due to the different integration times of the physics mode and the calibration mode, the recorded fraction of a SiPM signal may vary between the two modes. As a result, the observed IC_{cell} may deviate from IC_{ASIC}.

As explained in section 3.7, each individual SiPM has an optimal operation voltage. The high voltage (HV) power supplies only provide one voltage setting per half module. Thus, the VFE electronics need to adjust the voltages applied to each SiPM to achieve the optimal values.

The DAQ system contains Analogue to Digital Converters (ADCs), which digitise the multiplexed analogue signals from the ASICs. The ADCs are a part of the CALICE Readout Cards (CRCs). One ADC-channel corresponds to an input signal of 76 μV. The conversion from a signal A measured in units of ADC-channels to the charge released by the corresponding SiPM is done via

$$A\,[\mathrm{fC}] = A\,[\mathrm{ADC-ch.}] \cdot \frac{76\,\mu\mathrm{V}}{G_{PM}} \tag{3.3}$$

Chip	Sensor
0	1
1, 2, 3	2
4, 5, 6	3
8, 9, 10	4
11	5

Table 3.1: Assignment between readout chips and the temperature sensors closest to the SiPMs connected to the respective chips.

for physics mode operation. In calibration mode, an additional factor is needed to compensate for the possible signal losses due to the shorter integration time:

$$A\,[\mathrm{fC}] = A\,[\mathrm{ADC-ch.}] \cdot \frac{76\,\mu\mathrm{V}}{G_{CM}} \cdot \frac{IC_{ASIC}}{IC_{cell}}\,. \tag{3.4}$$

3.3 The Calibration and Monitoring System

The Calibration and Monitoring Boards [21] are connected to one side of the AHCAL module cassettes, as shown in figure 3.1. Each CMB contains 12 UV LEDs and 12 PIN photodiodes (Hamamatsu SFH250). Clear optical fibres guide the light from each LED to 18 scintillator tiles and to one of the PIN diodes, which monitors the LED light output. A CAN-BUS connection is used to steer the LEDs and to read the data from the temperature sensors inside the CMBs and the cassettes. Table 3.1 summarises which temperature sensor in each cassette is closest to the SiPMs read out by which chip of the VFE electronics (see section 3.2).

One application of the LED system is the gain calibration of the SiPMs. Recording the responses of the SiPMs to pulsed light of low intensity (1-5 generated photoelectrons) in calibration mode yields single pixel spectra. These spectra are used to determine the gain of each SiPM, as described in section 2.3.

In addition, response curves are generated by stepwise increasing the LED intensities and measuring the responses of the SiPMs at each setting. An explanation of response curves is given in section 2.3. Measuring response curves in physics mode and in calibration mode and dividing the SiPM signals at the same light intensities yields the intercalibration factors IC_{cell} of the cells (see section 3.2).

3.4 MIP Calibration

Muons acting as minimum ionising particles (MIPs) define the minimal energy depositions which can be measured by the AHCAL physics prototype. The response of a single SiPM to the scintillation light generated by the energy deposition of a muon in the corresponding

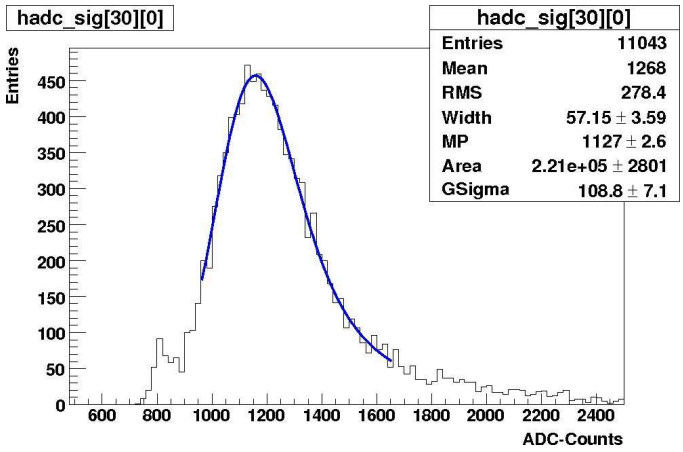

Figure 3.5: The response of a SiPM to muons depositing energy in a scintillator tile and the corresponding pedestal [26]. The Landau convoluted with a Gaussian fit is indicated by the solid line. The difference between the most probable value of this fit and the mean of the pedestal defines A^{MIP}.

scintillator tile is shown in figure 3.5. A small amount of pedestal events is displayed as reference. A Landau convoluted with a Gaussian fit is applied to determine the most probable value of the response, A^{MPV} [25]. A pure Gaussian fit yields mean A^{ped} and width σ^{ped} of the pedestal. The difference between A^{MPV} and A^{ped} defines the MIP response factor A^{MIP} of the SiPM. This factor is used for the calibration of all energy deposition measurements in this cell. The corresponding procedure is described in section 3.6. A determination of A^{MIP} for each cell of the physics prototype is necessary.

3.5 Light Yield

The light yield LY of a SiPM tile system is defined as the number of SiPM pixels firing when a single MIP deposits energy in the tile the SiPM is connected to, i.e. it is the ratio between the MIP response A^{MIP} and the gain G of a cell:

$$LY\,[\frac{\text{pix}}{\text{MIP}}] = \frac{A^{MIP}\,[\text{ADC} - \text{ch.}]}{G\,[\text{ADC} - \text{ch.}] \cdot IC_{cell}}\,. \tag{3.5}$$

Since G is determined in calibration mode and A^{MIP} in physics mode, G needs to be multiplied with the intercalibration factor IC_{cell} to correct for the different amplifications (see equation 3.2).

Both A^{MIP} and G depend on the bias voltage applied to the SiPM and on the operation temperature (see section 2.4). Thus, the light yield depends on these parameters as well.

The light yield is a measure of the detector performance. The detector performance is characterised by two factors, the signal to noise ratio and the dynamic range. The signal

to noise ratio is defined as the ratio between the amplitude of a measured signal and the width of the corresponding pedestal. The dynamic range is the difference between the largest and the smallest energy deposition that can be detected in a cell. A higher light yield is related to a larger signal to noise ratio, but a smaller dynamic range. According to studies performed during the construction of the AHCAL physics prototype, the best compromise between a high signal to noise ratio and a large dynamic range is achieved at a light yield of 15 $\frac{\text{pix}}{\text{MIP}}$ [19].

3.6 Energy Calibration

The calibration of energy depositions measured with the AHCAL physics prototype is done in several steps. First, the measured response $A_i\,[\text{ADC}-\text{ch.}]$ of each cell i is corrected for nonlinearity effects by multiplying it with the function $f_{sat}(A_i\,[\text{pix}])$. This function is the inverse of f_{pix} and is deduced from SiPM response curves measured on the bare SiPMs in a laboratory setup (see sections 2.3 and 3.7). The conversion from A_i given in ADC-channels to A_i in units of fired pixels is done by applying

$$A_i\,[\text{pix}] = \frac{A_i\,[\text{ADC}-\text{ch.}]}{G_i\,[\text{ADC}-\text{ch.}]\cdot IC_{cell,i}}\,. \tag{3.6}$$

The measurement of the gain G and the intercalibration factor IC_{cell} are described in section 3.3.

Dividing the corrected signal by the MIP response of the cell, A_i^{MIP}, gives the measured energy deposition in units of MIPs:

$$E_i\,[\text{MIP}] = \frac{A_i\,[\text{ADC}-\text{ch.}]}{A_i^{MIP}\,[\text{ADC}-\text{ch.}]}\cdot f_{sat}(A_i\,[\text{pix}])\,. \tag{3.7}$$

The determination of A^{MIP} is explained in section 3.4. The amount of energy deposited by a muon acting as a MIP in the scintillator material is extracted from MonteCarlo simulations. Multiplying $E_i\,[\text{MIP}]$ with this factor eventually yields the energy deposition in cell i in GeV.

As described in section 2.4, gain and response of a SiPM depend on bias voltage and temperature. In order to obtain an energy deposition in units of MIPs using equations 3.6 and 3.7, both G_i and A_i^{MIP} need to be known at the same operation conditions under which the signal A_i is measured.

3.7 SiPM Production and Characterisation

The CALICE AHCAL physics prototype uses 7608 SiPMs produced by the Moscow Engineering and Physics Institute (MEPHI) and Pulsar Enterprise [23]. The SiPMs consist of 34 x 34 pixels on an area of 1 mm^2. Typically, they have capacities of 50 fF and quenching

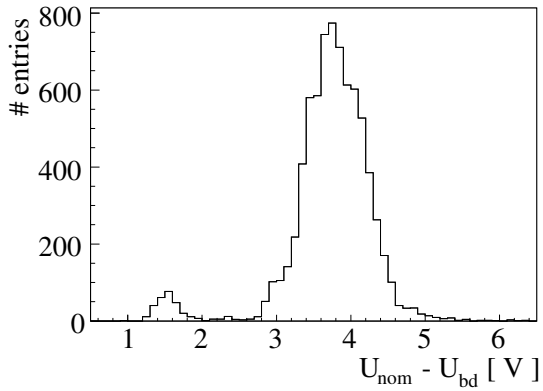

Figure 3.6: Differences between nominal bias voltage U_{nom} and breakdown voltage U_{bd} for the SiPMs used in the AHCAL physics prototype. There are two groups of different mean $U_{nom} - U_{bd}$, one at $U_{nom} - U_{bd} = 1.5\,\mathrm{V}$ and one at $U_{nom} - U_{bd} = 3.8\,\mathrm{V}$.

resistors of 2 to 20 MΩ. Thus, according to equation 2.1, the pixel recovery times are $100 - 1000\,\mathrm{ns}$. The gain within this SiPM sample ranges from $0.9 \cdot 10^6$ to $2.5 \cdot 10^6$. The devices are most sensitive to green light. Their geometrical efficiency ε^{Geo} is approximately $20 - 35\,\%$ and their Quantum Efficiency ε^{QE} is about $80\,\%$. They are operated at Geiger efficiencies ε^{Geiger} of $90 - 95\,\%$. As stated in [11], the variations of the gains of these SiPMs with bias voltage and temperature changes are $2.5\,\frac{\%}{100\mathrm{mV}}$ and $-1.7\,\frac{\%}{\mathrm{K}}$. The corresponding dependencies of the SiPM responses are quoted as $7\,\frac{\%}{100\mathrm{mV}}$ and $4.5\,\frac{\%}{\mathrm{K}}$.

Data from characterisation measurements performed on the bare SiPMs and on the combined SiPM tile systems by the Moscow Institute for Theoretical and Experimental Physics (ITEP) are available. The data include the nominal operation voltage for each SiPM. Figure 3.6 (left) shows the differences between the nominal operation voltages U_{nom} and the breakdown voltages U_{bd} for all SiPMs used in the AHCAL prototype. There are two groups of different mean $U_{nom} - U_{bd}$. The mean of the first group is 1.5 V, the mean of the second group is 3.8 V.

The nominal operation voltage is determined by illuminating a bare SiPM with LED light and varying the bias voltage of the SiPM. The light intensity is chosen to correspond to the light emitted by a scintillator tile after energy deposition by a MIP. The nominal operation voltage is the bias voltage that results in a SiPM response of 15 pixels to this light, i.e. in a light yield of $15\,\frac{\mathrm{pix}}{\mathrm{MIP}}$.

The results of light yield measurements performed on the combined SiPM tile systems including the wavelength-shifting fibres are presented in figure 3.7. The SiPMs are operated at their nominal voltages. The top left histogram summarises the results for all tiles used for the AHCAL prototype. The other three histograms include only tiles of one size. A ^{90}Sr source is used to generate the MIP like signals in the centres of the tiles. The light yield of all SiPM tile systems is $16.7\,\frac{\mathrm{pix}}{\mathrm{MIP}}$ with a spread of $3.7\,\frac{\mathrm{pix}}{\mathrm{MIP}}$. For the 3 x 3 cm^2 tiles, the mean is $16.8\,\frac{\mathrm{pix}}{\mathrm{MIP}}$ with a spread of $3.8\,\frac{\mathrm{pix}}{\mathrm{MIP}}$, for the 6 x 6 cm^2 tiles it is $17.2\,\frac{\mathrm{pix}}{\mathrm{MIP}}$ with a

spread of 3.5 $\frac{\text{pix}}{\text{MIP}}$ and for the 12 x 12 cm^2 tiles 13.4 $\frac{\text{pix}}{\text{MIP}}$ with a spread of 2 $\frac{\text{pix}}{\text{MIP}}$. The large spreads are caused by inhomogeneities in the tile samples and the WLS fibres. The light yield for tiles of different size diverges because the light collection efficiency varies with the tile size and the length and the positioning of the WLS fibre [27].

The characterisation measurements also include values for the gain, the response to LED light of fixed intensity, the crosstalk and the noise of each SiPM. The dependencies of these parameters on the bias voltage are given as well. In addition, response curves measured on the bare SiPMs are provided. These response curves show the saturation behaviour of the SiPMs and are used to correct for it. SiPM saturation and response curves are described in section 2.3. The curves are generated by measuring the responses of a SiPM to LED light of different intensities. A photomultiplier tube is used to quantify the light intensity. Figure 3.8 displays all response curves obtained at ITEP. The curves are normalised so that the slope between the second and the third measurement point is 1 for each SiPM. Thus, the values on the x-axis correspond to the theoretical number $N_{ph.e.}$ of firing pixels of a linear device, which is not subject to saturation.

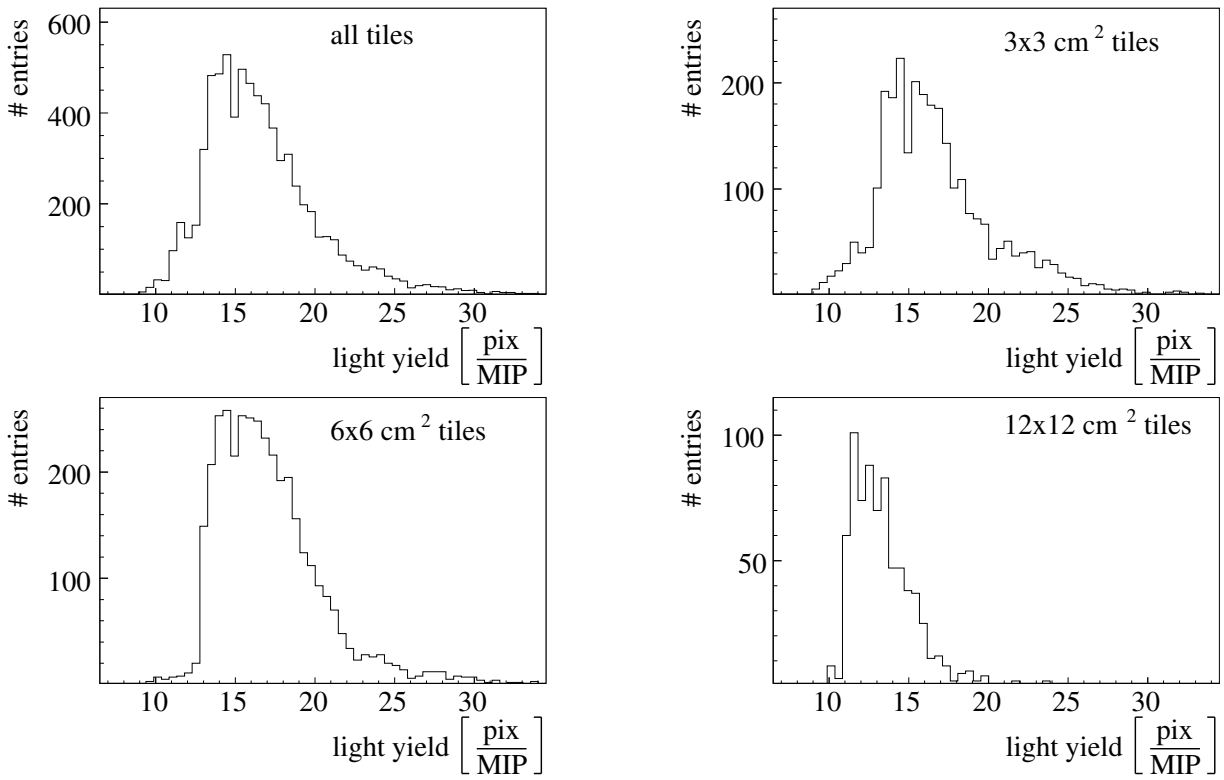

Figure 3.7: Light yields measured at ITEP using ^{90}Sr as a source of MIPs. Top left: All tile sizes (mean: 16.7 $\frac{\text{pix}}{\text{MIP}}$, spread: 3.7 $\frac{\text{pix}}{\text{MIP}}$). Top right: 3 x 3 cm^2 tiles (mean: 16.8 $\frac{\text{pix}}{\text{MIP}}$, spread: 3.8 $\frac{\text{pix}}{\text{MIP}}$). Bottom left: 6 x 6 cm^2 tiles (mean: 17.2 $\frac{\text{pix}}{\text{MIP}}$, spread: 3.5 $\frac{\text{pix}}{\text{MIP}}$). Bottom right: 12 x 12 cm^2 tiles (mean: 13.4 $\frac{\text{pix}}{\text{MIP}}$, spread: 2 $\frac{\text{pix}}{\text{MIP}}$).

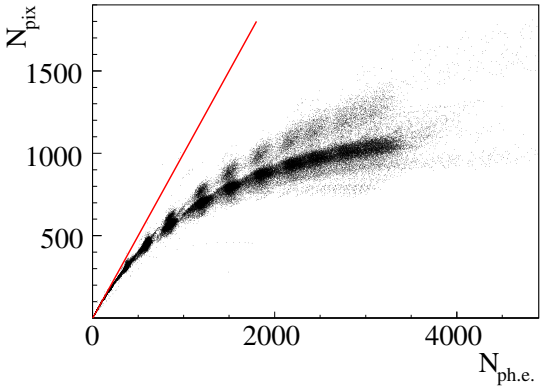

Figure 3.8: Response curves (dots) measured at ITEP for the SiPMs used in the AHCAL physics prototype. N_{pix} is the number of firing pixels, $N_{ph.e.}$ is proportional to the number of incident photons. The curves are normalised to have a slope of 1 between the second and the third measurement point. The solid line indicates the one to one correspondence.

Chapter 4

Investigation of SiPM Properties

The total response A of photodetectors operated in Geiger mode to incident light is a function of the photon detection efficiency ε and the gain G of the devices and the number N_γ of incoming photons (see chapter 2). This function is determined by the saturation behaviour of the photodetectors. In order to obtain the number of incident photons from a measured response, photon detection efficiency, gain and response curve of the used photodetector need to be known.

The saturation behaviour of a photodetector in Geiger mode depends on the effective number of pixels N_{eff}. This parameter is influenced by the width of incident light pulses and by the illuminated fraction of the detector surface. Thus, N_{eff} needs to be determined after including the photodetector in the final measurement setup.

Both the gain and the photon detection efficiency of a photodetector in Geiger mode depend on its operation voltage U_{bias} and on its temperature T, as described in section 2.4. As long as both operation voltage and temperature are stable, these parameters need to be determined only once. In the case of varying operation conditions, the changes of gain and photon detection efficiency need to be monitored. There are two methods to do this. The first method re-determines both parameters each time that a change in voltage or temperature occurs and yields status information for the photodetector with the best accuracy possible. The second method monitors the variations of bias voltage and temperature and calculates the corresponding changes of gain and photon detection efficiency. This second method requires the prior knowledge of the voltage and temperature dependencies of the gain and the photon detection efficiency of the photodetector. Therefore, it suffers from uncertainties of the voltage and temperature measurements and of the determination of the corresponding dependencies. On the other hand, monitoring voltage and temperature is much less complex and time-consuming than measuring the gain and the photon detection efficiency repeatedly. Thus, both methods have advantages and disadvantages.

As mentioned in chapter 3, the CALICE AHCAL physics prototype uses 7608 SiPMs to detect light from single scintillator tiles. The following sections summarise the results of measuring the effective number of pixels and the voltage and temperature dependencies of the gain and the response to light of fixed amplitude of these SiPMs. The systematic

uncertainties of these dependencies are quantified. All measurements described are performed on the fully assembled AHCAL physics prototype. The outcomes are compared to reference values obtained in a laboratory setup prior to the mounting of the SiPMs on the scintillator tiles (see section 2.4). All fits and calculations of fit probabilities and correlation factors are performed using the ROOT analysis framework (version 5.16) [28]. The standard deviation of the centre 90 % of the normally distributed entries of a histogram is called σ_{90}. Using σ_{90} instead of the standard deviation calculated from all entries removes the impact of long tails and outliers.

4.1 Effective Number of Pixels

As described in section 2.3, photodetectors operated in Geiger mode are non-linear devices and saturation effects have to be taken into account. The saturation behaviour is controlled by the effective number of pixels N_{eff} of a photodetector, which can be extracted from a response curve. This curve represents the response $A(N_\gamma)$ of a photodetector to incident light of different intensities N_γ. The part of a response curve approaching saturation can be approximated by the function given in equation 2.4. Because of non-uniformities in the distribution of the light hitting the photodetector, this simple function does not describe a response curve at all light intensities well. But the function is sufficient to perform a fit on the last data points close to saturation to extract N_{eff}.

4.1.1 Response Curves Measured on the SiPM-Tile Systems

Several response curves $A(x)$ for the SiPMs used in the AHCAL physics prototype are measured. The SiPMs are mounted on scintillator tiles and illuminated by LEDs via wavelength-shifting fibres (see sections 3.1 and 3.3). The SiPM signal A is the mean value of a distribution of the response of a SiPM to light of intensity x. The spread of this distributions divided by the square root of the numbers of entries is the statistical error on A. The results are calibrated in numbers of firing pixels using equation 3.6. For this calibration, gain values determined at the same temperature as the respective response curves are chosen. Single gain measurements have a relative uncertainty of $\approx 0.7\,\%$ (see section 5.3.1). This uncertainty contributes to the systematic errors of the calibrated response values. Since this error is correlated for all points of a response curve, it only affects the result for N_{eff} and is neglected during the fitting procedure. An intercalibration factor averaged over one month is applied. Because intercalibration factors do not change with operation conditions, averaging them over several measurements does not introduce additional errors.

To quantify the light intensity x of the LEDs illuminating the SiPMs, a parameter is chosen which is proportional to the voltages applied to the LEDs. While the relation between LED light intensity and LED current is linear, the relation between intensity and applied voltage is not. This non-linearity has no effect on the extraction of the effective

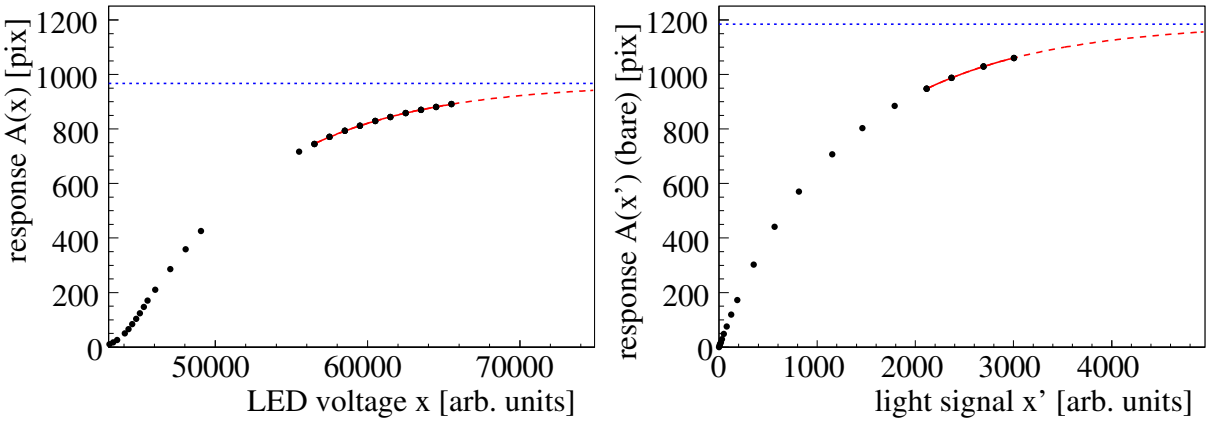

Figure 4.1: Two response curves measured for the same SiPM, once mounted on a tile and illuminated via a wavelength-shifting fibre (left), and once in its bare state (right). The fit to the last 10 (left) or 4 (right) points (solid line), its extrapolation to higher light intensities (dashed line) and N_{eff} (dotted line) are displayed as well.

number of pixels and can thus be neglected for the studies described in this section. A way to avoid the non-linearity is to use the readout of the PIN diodes included in the CMB boards to measure the light intensity instead (see section 3.3). Since x is not equal to the number N_γ of incident photons, the function in equation 2.4 is modified to describe the measured curve $A(x)$:

$$A(x) = N_{eff} \cdot (1 - \mathrm{e}^{-(x+c_2)\cdot c_1}) \cdot G \; . \tag{4.1}$$

As mentioned before, these studies only aim for the determination of N_{eff}, which is not affected by these changes. The parameters c_1 and c_2 are needed to describe $A(x)$. They have no impact on N_{eff} and are not discussed further.

The dots in figure 4.1 (left) display a response curve measured for one of the AHCAL SiPMs with the fully assembled physics prototype. The statistical errors are too small to be observed. The deviation of the response curve from the expected linear shape for low light intensities is caused by the non-linear relation between the LED light and the parameter x used to quantify it.

The effective number of pixels of a single SiPM extracted from performing a fit on a different number of points of a response curve is shown in figure 4.2 (left). The result varies by less than 1 % from 8 to 13 used points. Both the error on each fit result and the number of good fits, i.e. the number of fits with probability larger than 10^{-3}, decrease with an increasing number of chosen points. For the following studies, the fits are performed on the last 10 points of the response curves. This choice is motivated by the observation that this is the highest number of fit points for which still good fit results are obtained for more than 4500 SiPMs. The corresponding fit is displayed by the solid line in figure 4.1 (left). The extrapolation to higher intensities is indicated by the dashed line. Figure 4.2 (right) shows the relative difference between the results N_{eff}^{10} and N_{eff}^{9} obtained from applying the fit to the last 10 and 9 data points of a single measurement. All 4729 AHCAL SiPMs

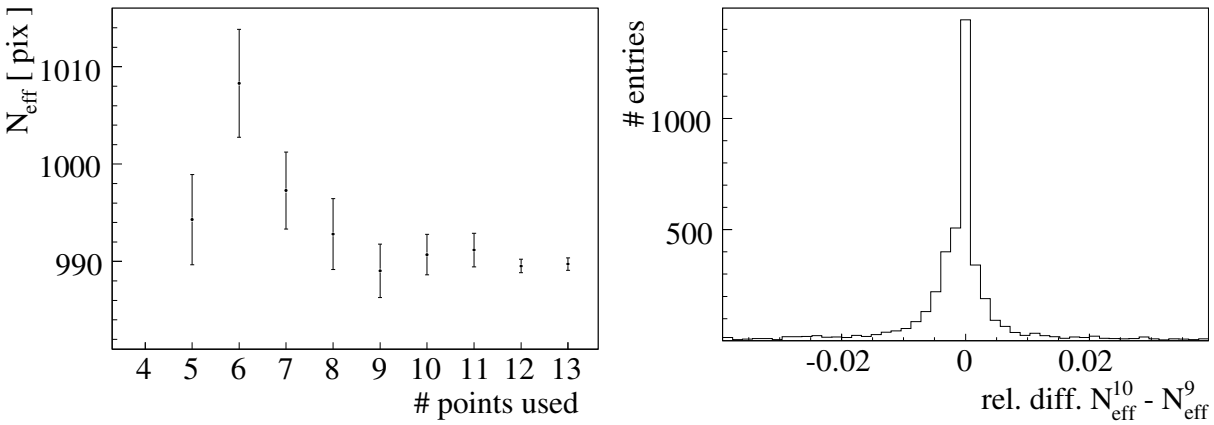

Figure 4.2: (left) The results for the effective number of pixels of a SiPM depending on the number of points included in the fitting procedure. (right) The relative difference between the results for N_{eff} obtained using 10 or 9 points to perform the fit on.

for which the fit probability is larger than 10^{-3} are included. The mean value is at zero, the σ_{90} is 0.9 %. This uncertainty is an estimate of the systematic error σ_{fit} introduced by choosing only a certain number of data points for the fit.

For each SiPM, the mean $\overline{N}_{eff}$ from 30 response curve measurements i is determined. Figure 4.3 (left) shows the the relative difference between N^i_{eff} and $\overline{N}_{eff}$ for a single measurement set i. The σ_{90} of this difference is $\sigma_{meas} = 2.2\,\%$, which is the relative uncertainty of a single measurement. Since the means are calculated from 30 measurements, the error σ_{mean} on these means is $\frac{\sigma_{meas}}{\sqrt{30-1}} = 0.4\,\%$ for each SiPM. Adding this uncertainity to σ_{fit} yields the total error on the obtained numbers of effective pixels, $\sigma_{tot} = \sqrt{\sigma^2_{fit} + \sigma^2_{mean}}$. It is about 1 %.

4.1.2 Response Curves Measured on the Bare SiPMs

Figure 4.1 (right) shows a response curve $A(x')$ obtained in a laboratory setup using a bare SiPM (see section 3.7). The light intensity x' is measured by a PMT. The first data point is fixed to $(0, 0)$. The values of x' are scaled to yield a slope of 1 between the second and the third data point. Thus, the unit of x' corresponds to the number of firing pixels expected for a linear device. The uncertainty of the gain calibration only shifts the whole curve, but does not contribute to the errors of individual points. The statistical error σ_s is the same for all data points. Because σ_s is not known for these measurements, it needs to be estimated. Saturation effects are neglegible for low light intensities. Thus, the second to fourth data points, $A(x'_2)$, $A(x'_3)$ and $A(x'_4)$, are expected to lie on a straight line, as shown in figure 4.4. The unscaled x' values are used, i.e. the slope between $(x'_2, f(x'_2))$ and $(x'_3, f(x'_3))$ is not fixed to 1. The distances between x'_2 and x'_3 and between x'_3 and x'_4 are

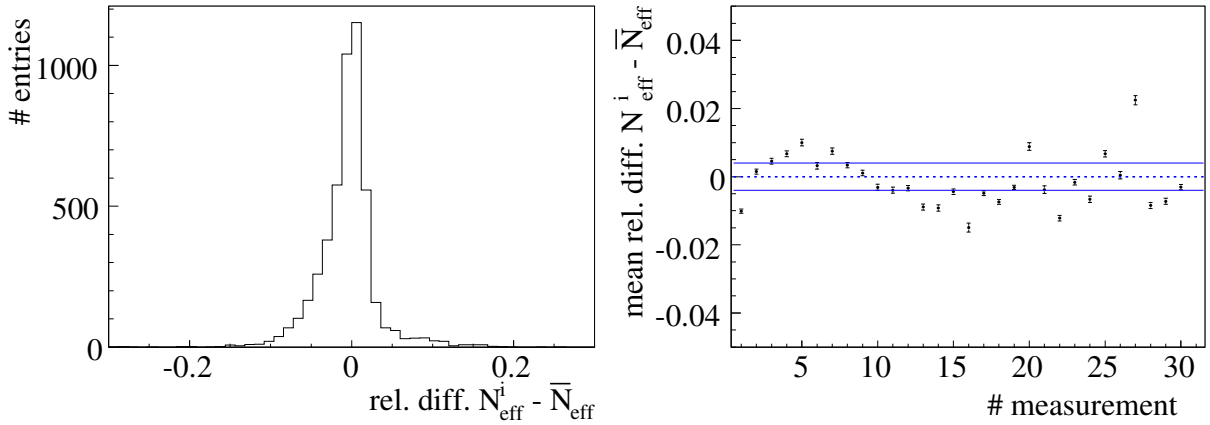

Figure 4.3: (left) Relative difference N^i_{eff} - $\overline{N}_{eff}$. The values N^i_{eff} are the results from a single set of response curve measurements, $\overline{N}_{eff}$ is the mean of 30 measurements. (right) Means of the relative differences between single measurements N^i_{eff} and the mean value $\overline{N}_{eff}$ for 30 measurements. The errors are the statistical errors of the means. The solid lines indicate the $1\sigma_{mean}$ range around the dotted line at $N^i_{eff} - \overline{N}_{eff} = 0$.

equal. To estimate σ_s, an expected value

$$A_c(x'_3) = A(x'_2) + \frac{A(x'_4) - A(x'_2)}{x'_4 - x'_2} \cdot (x'_3 - x'_2) \tag{4.2}$$

is calculated. The spread of the difference $A(x'_3) - A_c(x'_3)$ is the observed error σ_{obs}. The statistical errors of all three data points, $A(x'_2)$, $A(x'_3)$ and $A(x'_4)$, contribute to σ_{obs}. The relation between σ_{obs} and σ_s is approximated by

$$\sigma_s = \sqrt{\frac{2}{3}} \cdot \sigma_{obs} \ . \tag{4.3}$$

According to this procedure, σ_s is about 0.1 pixel.

The fit of the function $A(x)$ from equation 4.1 performed on the last four data points of the curve in figure 4.1 (right) is presented by the solid line. Again, the dashed line indicates the extrapolation to higher light intensities. The value of N_{eff} extracted from this fit is marked by the dotted line. The choice of using only the last four data points for the fits are based on considerations analogue to those made for the response curves measured with the fully assembled prototype. For the laboratory setup measurements, the uncertainty introduced by manually choosing the number of points used for the fit is $\sigma'_{fit} = 0.2\,\%$.

Response curves measured before tile mounting are available for 7596 out of 7608 SiPMs. The fits performed on the last four points yield results with fit probabilities larger than 10^{-3} for 5499 of them. Only these results are used for further studies.

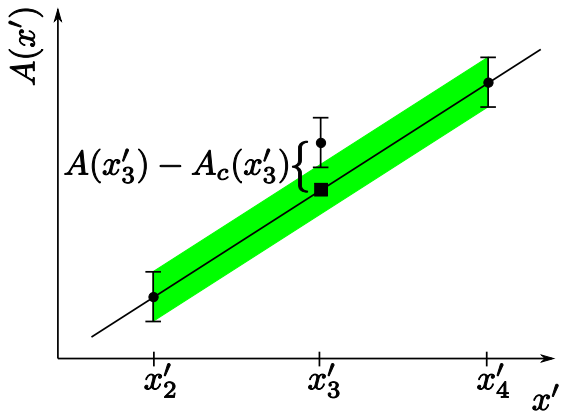

Figure 4.4: Estimation of statistical errors on data points obtained in a laboratory setup for the bare SiPMs.

4.1.3 Comparison Between N_{eff} Before and After Tile Mounting

Comparing the two curves in figures 4.1 (left) and (right) indicates that the effective number of pixels yielded for the same SiPM with two different measurement setups deviates by approximately 20 %. Figure 4.5 (left) shows the correlation between the effective number of pixels determined for the SiPMs mounted on the tiles and the same value obtained for the bare SiPMs. The correlation factor is 21 %. The mean ratio $\frac{N_{eff}^{mounted}}{N_{eff}^{bare}}$ is 81 % with a spread of 9 % within the SiPM sample, as shown in figure 4.5 (right). This agrees with the previous observation from figures 4.1 (left) and (right). The reason for the decrease in the number of effective pixels is that after assembly, a SiPM is illuminated via the wavelength-shifting fibre, which has a diameter of 1 mm. Thus, not the whole SiPM surface of 1 mm^2 can be illuminated, which reduces the maximum number of physical pixels that contribute to the signal generation.

In principle, differences in the LED systems used for the two measurements could also account for this deviation. The width of the light pulse influences the possible firing frequency of each pixel during the pulse and thus the effective number of pixels. But since both the measurements on the bare and on the mounted SiPMs are done with the same LED pulse lengths of 10 ns, which is much shorter than the recovery times of > 100 ns of the SiPMs, this cannot explain the deviations observed in figure 4.5 (left).

Figure 4.5 (left) exhibits a significant tail of the results of N_{eff} for the bare SiPMs to higher pixel numbers. All SiPMs in this tail originate from the same production period. The tail is the result of different quenching resistors used for the pixels of the SiPMs during this production period. Lower quenching resistors decrease the recovery time of SiPM pixels, so that they can fire more often during a light pulse of fixed width. This increases the effective number of pixels.

Differences in the relative positioning of SiPMs and wavelength-shifting fibres influence the part of the SiPMs the fibres can illuminate for each SiPM individually. Thus, in the

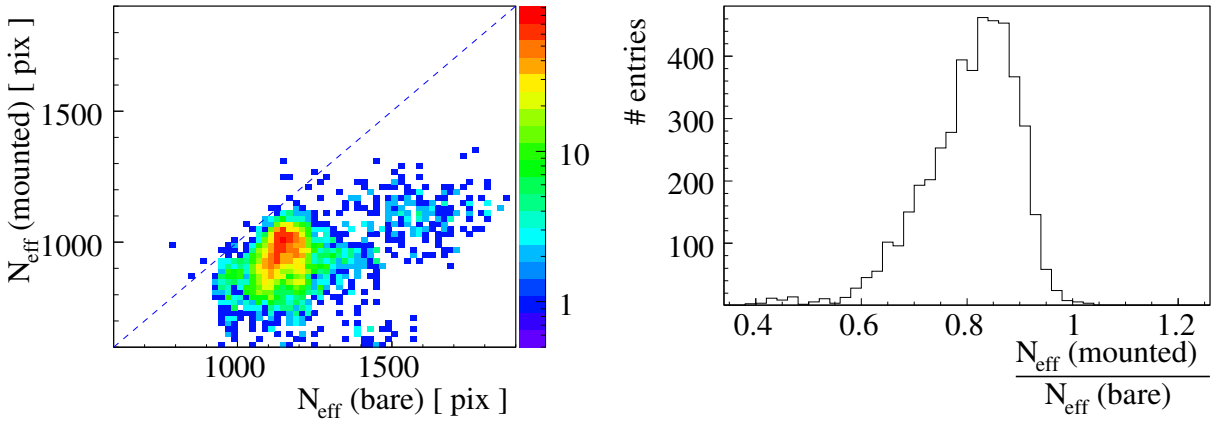

Figure 4.5: (left) Correlation between N_{eff}^{bare} before and $N_{eff}^{mounted}$ after mounting the SiPMs on the tiles and assembling the AHCAL physics prototype. (right) Ratio between $N_{eff}^{mounted}$ and N_{eff}^{bare}. In average, $N_{eff}^{mounted}$ is 19 % smaller than N_{eff}^{bare}.

case of the mounted SiPMs, N_{eff} is subject to additional fluctuations from one SiPM to another, which contributes to the low correlation between the results obtained from the measurements performed with the two setups.

4.1.4 Rescaling of Response Curves

For the correction of SiPM saturation effects, not only the effective total number of pixels is needed, but the whole response curve itself. Taking the result from the previous sections into account, these curves should be recorded with the final operation setup. However, it is usually easier and more accurate to perform these measurements under controlled laboratory conditions. A possible option is to use the curves obtained before mounting the SiPMs on the tiles and to rescale them with a factor $\frac{N_{eff}^{mounted}}{N_{eff}^{bare}}$. This factor corrects for the different effective numbers of pixels. The effective number of pixels $N_{eff}^{mounted}$ is measured with the final setup, while N_{eff}^{bare} is the result obtained for the bare SiPMs. Using the measurements described above, the uncertainty on each of these ratios is about $\sqrt{(\sigma_{tot})^2 + (\sigma'_{fit})^2} = 1\,\%$. Whether these rescaled curves really describe the saturation behaviour of the mounted SiPMs correctly is subject of ongoing studies [29].

4.2 Voltage and Temperature Dependencies of the Gain and the Response

The gain G of a photodetector operated in Geiger mode is proportional to the difference between the applied bias voltage U_{bias} and the breakdown voltage U_{bd} of the device, as

explained in section 2.4. Gains are obtained by recording single pixel spectra and calculating the difference between the means of two neighbouring peaks (see section 2.3). The slope of a linear fit performed on gains determined at different bias voltages quantifies the gain voltage dependence, assuming that the temperature stays constant during the measurements. The breakdown voltage, and consequently the gain, depends linearly on the operation temperature T of the photodetector. A linear fit performed on the results of several gain measurements collected at the same bias voltage but at different temperatures yields the strength of this dependence.

The relations between variations of the operation voltage or the temperature of a photodetector in Geiger mode and changes of the response A of the photodetector to light of fixed intensity are approximately linear, as long as the variations do not exceed a few 100 mV or K. These dependencies are quantified the same way as the corresponding gain dependencies.

4.2.1 Voltage Dependence of the Gain

For the SiPMs in the fully assembled AHCAL physics prototype, results from two voltage scans are available. The first scan covers a range of 1 V at an average prototype temperature of 25 °C, which varies by less than 0.5 °C. In the course of the second scan extending over 1.2 V the temperature increases by approximately 1 °C. Here, the average temperature is 27 °C. Within these voltage ranges, the gains vary by approximately 30 %. Figure 4.6 shows the gain of a single SiPM at different bias voltages. The results from the first set of measurements are indicated by the triangles, the results from the second set are presented by the dots. As expected, the gain G is proportional to the applied bias voltage U_{bias}. In addition, the gain at a fixed bias voltage is lower for higher temperature, which also matches the expectation.

Independent fits are performed on the values from both measurement sets. Figure 4.7 shows the $\frac{\chi^2}{DOF}$ distributions of these fits. All fit results with $\frac{\chi^2}{NDF} < 10$ are regarded as good. The others are neglected for further studies. From the first voltage scan at 25 °C, good fit results are obtained for 5389 SiPMs. The second scan at 27 °C yields 6352 good values. The large discrepancy between these two numbers is caused by the malfunction of four CMBs during the first measurements, as a result of which the gains of 864 SiPMs are missing for that period.

The correlation between the results from two independent determinations of $\frac{\mathrm{d}G}{\mathrm{d}U}$ with the same setup but at different temperatures is 97 %, as shown in figure 4.8 (left). Each dot represents the results for one SiPM of the studied sample. The dashed line indicates the one to one correspondence. The strong correlation demonstrates that the absolute voltage dependence of the gain is the same at different temperatures.

According to the results obtained at 27 °C, the mean relative gain voltage dependence $\frac{1}{G}\frac{\mathrm{d}G}{\mathrm{d}U}$ is 2.6 $\frac{\%}{100\mathrm{mV}}$ for the AHCAL SiPM sample, which matches the value of 2.5 $\frac{\%}{100\mathrm{mV}}$ quoted in [11] very well. The spread within the studied sample is 0.3 $\frac{\%}{100\mathrm{mV}}$, or 12 %. Considering

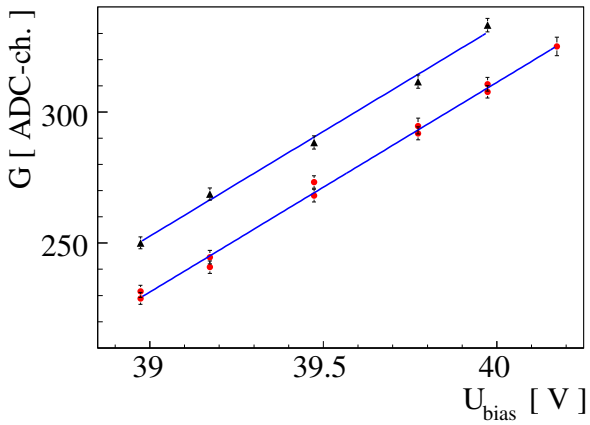

Figure 4.6: The gain G of one SiPM at different bias voltages U_{bias} measured at 25 °C (triangles) and at 27 °C (dots). The gain increases with U_{bias}, while the values at 25 °C are larger than those at 27 °C. The linear fits to both sets are indicated by the solid lines.

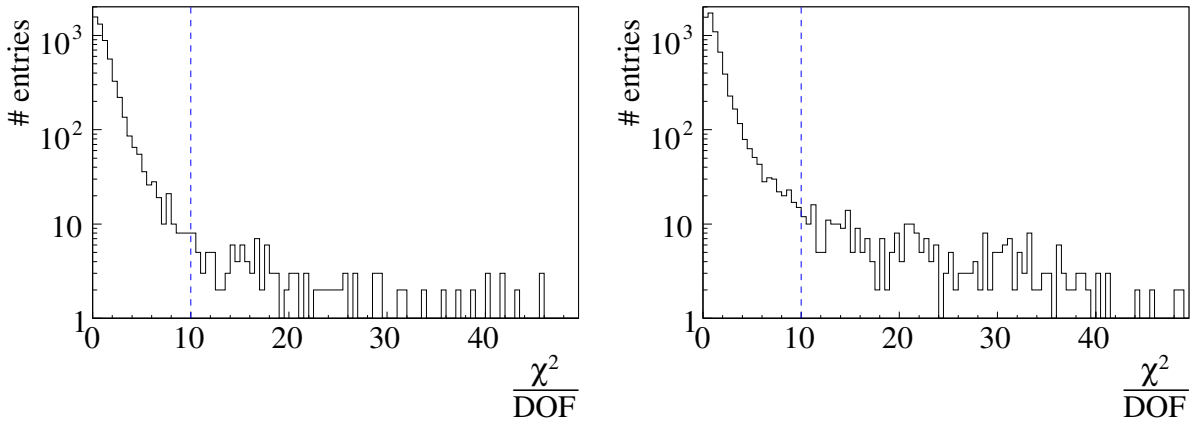

Figure 4.7: $\frac{\chi^2}{DOF}$ distributions from the measurements at 25 °C (left) and from the measurements at 27 °C (right). The lines mark the quality cut at $\frac{\chi^2}{DOF} = 10$.

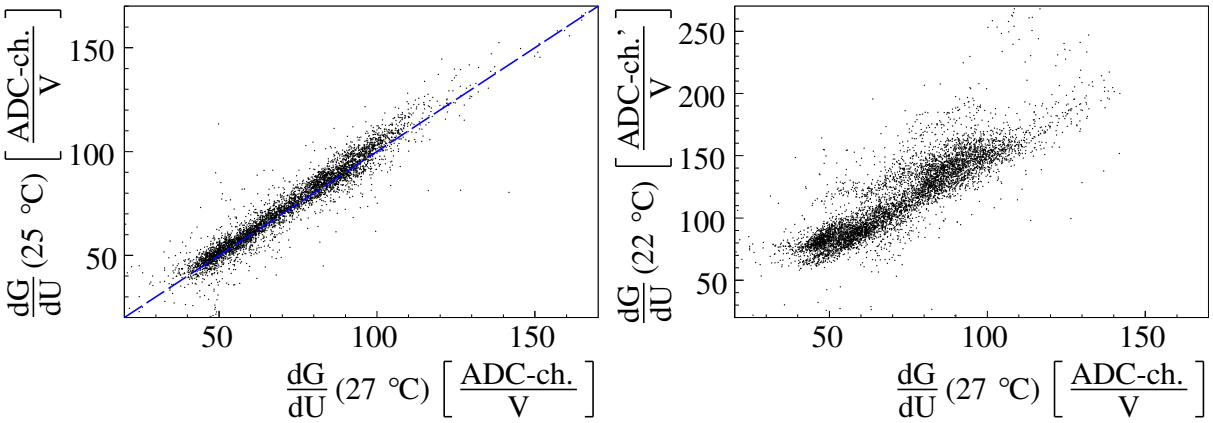

Figure 4.8: (left) Correlation between the results for $\frac{\mathrm{d}G}{\mathrm{d}U}$ from the measurements performed at 25 °C and at 27 °C with the same setup. The dashed line is the one to one correspondence. (right) Correlation between the results for $\frac{1}{G}\frac{\mathrm{d}G}{\mathrm{d}U}$ from the measurements performed at 27 °C using the assembled prototype and those performed at 22 °C on the bare SiPMs.

this spread, the voltage dependencies of the gains have to be measured and stored for each SiPM individually, instead of using a single mean for all devices.

The σ_{90} of the differences between the results for $\frac{1}{G}\frac{\mathrm{d}G}{\mathrm{d}U}$ from the two independent measurement sets is $0.1\,\frac{\%}{100\mathrm{mV}}$, which quantifies the systematic uncertainty on each of the determined slopes and corresponds to a relative uncertainty of 4 %. The small temperature changes which occur during the measurements and are neglected influence the outcoming slopes and contribute to this uncertainty.

Figure 4.8 (right) shows the correlation between the dependencies $\frac{\mathrm{d}G}{\mathrm{d}U}$ obtained from the measurements at 27 °C with the fully assembled AHCAL prototype and the corresponding results from measurements performed on the bare SiPMs at an average temperature of 22 °C (see section 3.7). The correlation is 87 %. This confirms the reproducibility of the gain voltage dependencies. The absolute values of the slopes deviate because different data acquisition systems with unequal ADC-channel scales are used for the measurements compared.

4.2.2 Temperature Dependence of the Gain

Two collections of gains measured at different temperatures are analysed, both acquired using the fully assembled AHCAL physics prototype. Within the first set, the average calorimeter temperature varies between 25 °C and 28 °C. The second set covers the range from 22 °C to 28 °C. For some SiPMs, the bias voltages applied during the first measurement period (U_{bias}^{mod}) are higher than the bias voltages used during the second (U_{bias}). Figure 4.9 presents the data for one SiPM from both sets as an example. The bias voltage of this SiPM is 0.5 V larger during set one than during set two. Because of this, the gains from the first set, depicted by the triangles, lie above the values from the second set, rep-

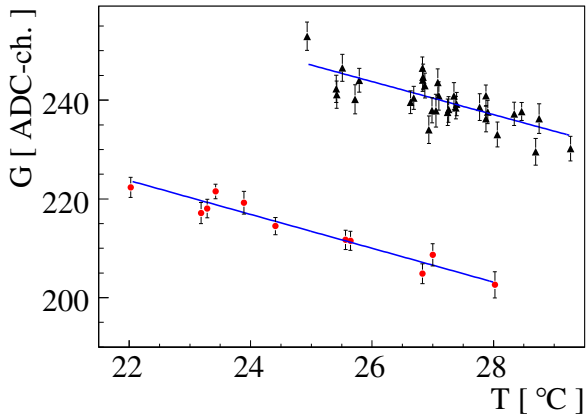

Figure 4.9: The gain G measured at different temperatures T at two fixed bias voltages (triangles: $U_{bias}^{mod} = 41.1\,\mathrm{V}$, dots: $U_{bias} = 40.6\,\mathrm{V}$). The lines indicate the linear fits.

resented by the dots, at the same temperature. As expected, the gain G decreases with rising temperature T in both cases.

Linear fits are performed on the data from both gain collections to extract the temperature dependencies of the gains, $\frac{\mathrm{d}G}{\mathrm{d}T}$. SiPMs for which the available gains do not cover a temperature range of at least 2 °C are omitted. The fits are indicated by the solid lines in figure 4.9. The $\frac{\chi^2}{DOF}$ distribution of all fits is displayed in figure 4.10. From the first data set, 6227 fit results and from the second set 6823 fit results with with $\frac{\chi^2}{DOF} < 20$ are regarded as good.

Figure 4.11 displays the 83 % correlation between the results for $\frac{\mathrm{d}G}{\mathrm{d}T}$ obtained from the two independent measurement sets. According to the results from the second set, the mean $\frac{1}{G}\frac{\mathrm{d}G}{\mathrm{d}T}$ of the AHCAL SiPM sample is $-1.7\,\frac{\%}{\mathrm{K}}$ with a spread of $0.3\,\frac{\%}{\mathrm{K}}$ within the sample, which

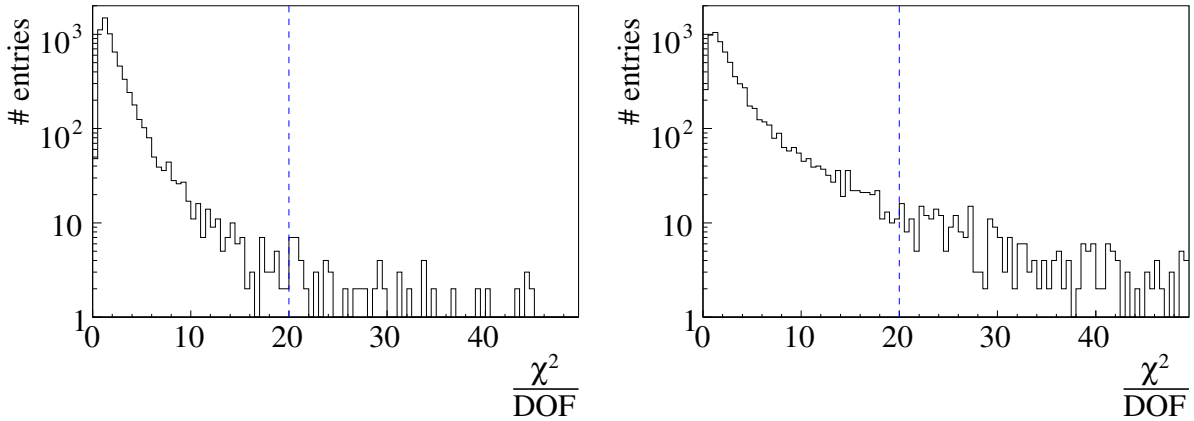

Figure 4.10: $\frac{\chi^2}{DOF}$ distributions from the first measurement set at U_{bias}^{mod} (left) and from the second set at U_{bias} (right). The lines indicate the quality cut at $\frac{\chi^2}{DOF} = 20$.

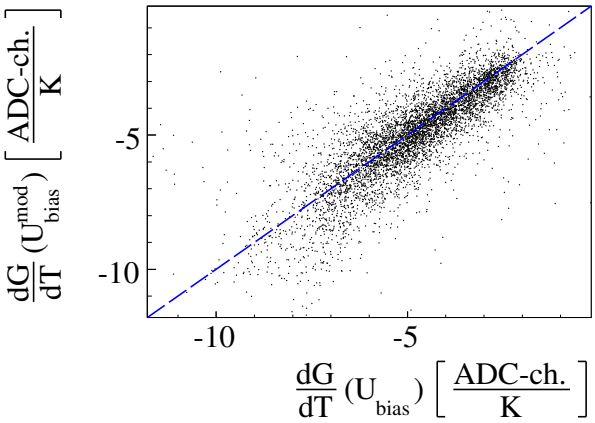

Figure 4.11: Correlation between the results for $\frac{dG}{dT}$ from the two sets of measurements collected at different voltages. The dashed line is the one to one correspondence.

corresponds to a relative spread of 18 %. The mean is equal to the result quoted in [11]. As for voltage dependencies of the gains, the spread of the temperature dependencies of the gains is too large to replace individual values for each SiPM by one mean.

The systematic uncertainty of the determined relative gain temperature dependencies is given by the σ_{90} of the differences between the results extracted from the two data sets. It is $0.2\,\frac{\%}{\mathrm{K}}$, or 12 %.

The correlation between the results for $\frac{dG}{dT}$ from the two measurement periods is lower than the correlation between the two extractions of $\frac{dG}{dU}$. In addition, the systematic error is larger for $\frac{1}{G}\frac{dG}{dT}$ than for $\frac{1}{G}\frac{dG}{dU}$. The major reason for the worse stability of the outcomes for the temperature dependencies of the gains is the uncertainty of the temperature measurements themselves. In the setup used, the temperature is not known for each SiPM individually, but is measured only at five positions in each module, as described in section 3.1. In addition, the response times of temperature sensors and SiPMs to changes in their environmental temperature are different. Although the temperature sensors are read out only every five minutes, they adapt faster to varying temperatures than the SiPMs do, since the latter are surrounded by insulating plastic. This different response times cause hysteresis effects when the temperature drops and rises again [22]. Measuring the gain at different temperatures during one continuous increase or decrease of temperature leads to better results than a fluctuating temperature. The data of the first set are collected during one month of increasing and decreasing environmental temperature. The data of set two cover only one week of continuously decreasing temperature. An additional increase in spread between the two determinations of $\frac{1}{G}\frac{dG}{dT}$ results from the bias voltage shift between the two data sets, which is not the same for all modules.

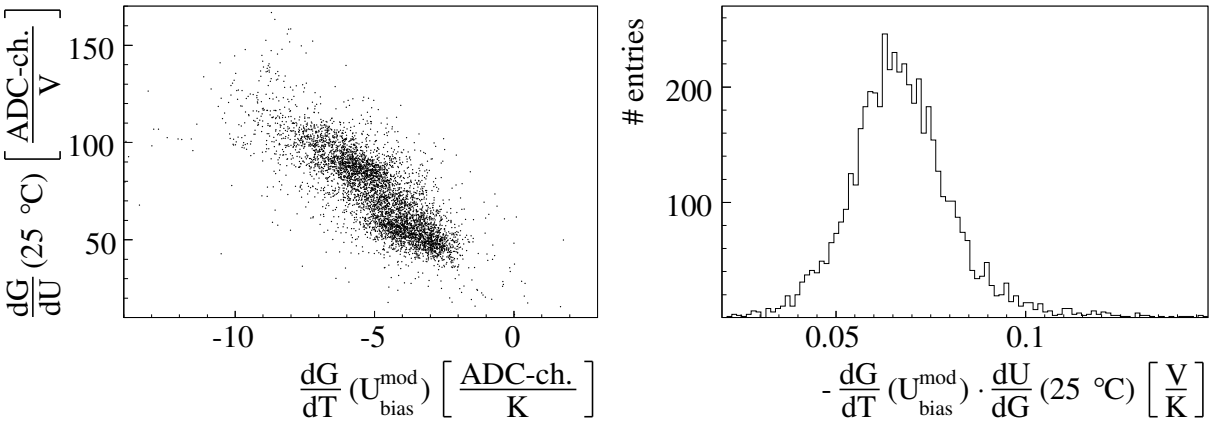

Figure 4.12: (left) Correlation between $\frac{\mathrm{d}G}{\mathrm{d}U}$ and $\frac{\mathrm{d}G}{\mathrm{d}T}$. (right) The negative ratio between $\frac{\mathrm{d}G}{\mathrm{d}T}$ and $\frac{\mathrm{d}G}{\mathrm{d}U}$, which corresponds to $\frac{\mathrm{d}U_{bd}}{\mathrm{d}T}$.

4.2.3 Temperature Dependence of the Breakdown Voltage

Voltage and temperature dependence of the gain of photodetectors operated in Geiger mode are related via the temperature dependence of the breakdown voltage, $\frac{\mathrm{d}U_{bd}}{\mathrm{d}T}$ (see section 2.4). Thus, the results for $\frac{\mathrm{d}G}{\mathrm{d}U}$ given in section 4.2.1 and the results for $\frac{\mathrm{d}G}{\mathrm{d}T}$ given in section 4.2.2 are expected to be correlated. The negative ratio between the two values should yield $\frac{\mathrm{d}U_{bd}}{\mathrm{d}T}$.

Figure 4.12 (left) shows the $-76\,\%$ correlation between $\frac{\mathrm{d}G}{\mathrm{d}U}$ determined at $25\,^{\circ}\mathrm{C}$ and $\frac{\mathrm{d}G}{\mathrm{d}T}$ from the first data set at increased bias voltages. The negative ratios $-\frac{\mathrm{d}G}{\mathrm{d}T} \cdot \frac{\mathrm{d}U}{\mathrm{d}G}$ are displayed in figure 4.12 (right). The mean is $67\,\frac{\mathrm{mV}}{\mathrm{K}}$ with a spread of $10\,\frac{\mathrm{mV}}{\mathrm{K}}$ within the sample of studied SiPMs. Using $\frac{\mathrm{d}G}{\mathrm{d}U}$ from the measurements at $27\,^{\circ}\mathrm{C}$ and $\frac{\mathrm{d}G}{\mathrm{d}T}$ from the second data set yields a mean of $65\,\frac{\mathrm{mV}}{\mathrm{K}}$ with a spread of $11\,\frac{\mathrm{mV}}{\mathrm{K}}$ between the single SiPMs.

The σ_{90} of the difference between the results from the two combinations of extracted voltage and temperature dependencies, i.e. the systematic uncertainty on the obtained $\frac{\mathrm{d}U_{bd}}{\mathrm{d}T}$ values, is $9\,\frac{\mathrm{mV}}{\mathrm{K}}$ and corresponds to a relative error of $13\,\%$. This error is consistent with the relative errors of the gain voltage and gain temperature dependencies added in quadrature.

The result matches the value of $\frac{\mathrm{d}U_{bd}}{\mathrm{d}T} = 56.0 \pm 0.1\,\frac{\mathrm{mV}}{\mathrm{K}}$ quoted in section 2.4 for an MPPC within one standard deviation. The obtained gain voltage and gain temperature dependencies of the AHCAL SiPMs are consistent.

4.2.4 Voltage Dependence of the Response

In order to study the voltage dependence of the response of the SiPMs used in the AHCAL physics prototype, the SiPMs are illuminated with light of fixed amplitude. The LED calibration system of the prototype, which is described in section 3.3, is used for this. The amplitudes of the LEDs are tuned to generate response signals which can be well separated

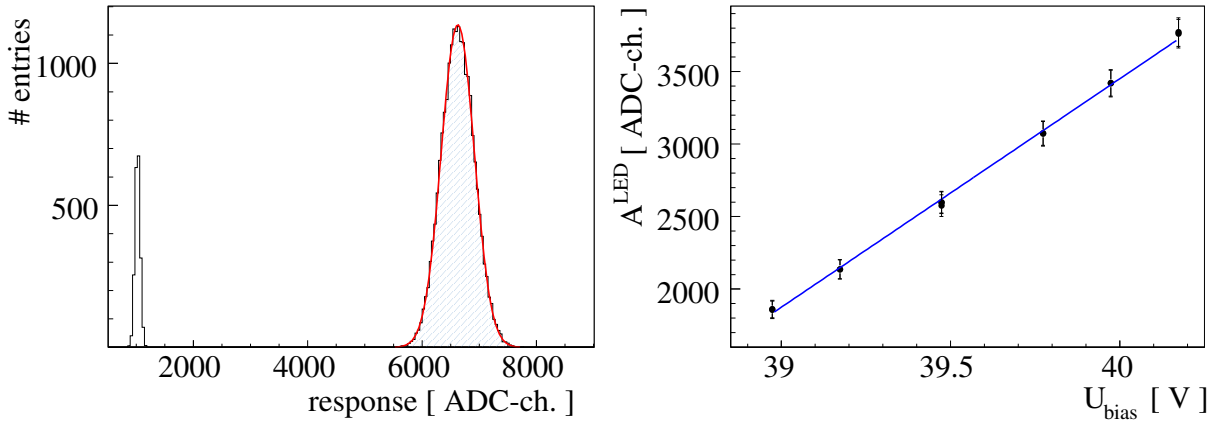

Figure 4.13: (left) The response to an LED signal for one SiPM (shaded histogram), including the Gaussian fit and the pedestal (open histogram). (right) The pedestal subtracted response A^{LED} to an LED signal of fixed intensity (dots) at different voltages U_{bias} and the linear fit performed on these data (solid line).

from the pedestals, but which are still small enough to keep saturation effects negligible. The response values are extracted from the measurements by performing a Gaussian fit on the recorded histograms. Afterwards the means of the pedestals are subtracted from the means obtained from the fits. This yields the response A^{LED}. Figure 4.13 (left) shows the response of one cell, including the Gaussian fit and the corresponding pedestal. The response of the illuminated SiPMs is measured at different bias voltages U_{bias}. This is done at an average calorimeter temperature increasing from 24.9 °C to 25.2 °C. Figure 4.13 (right) displays the outcome for one SiPM. As expected, the response increases linearly with the bias voltage.

Using a probability larger than 10^{-3} as criterion for good results of the linear fits, the voltage dependence $\frac{1}{A^{LED}}\frac{\mathrm{d}A^{LED}}{\mathrm{d}U}$ is successfully obtained for 5917 of 7608 SiPMs. Figure 4.14 (left) illustrates the 80 % correlation between these results and those from the measurements using the bare SiPMs, LED light of a different amplitude and a different data acquisition system. The absolute slopes depend on the number N_γ of incoming photons, i.e. on the amplitudes of the responses themselves ($A^{LED} \propto N_\gamma$, $\frac{\mathrm{d}A^{LED}}{\mathrm{d}U} \propto N_\gamma$). Because of this, only the relative values $\frac{1}{A^{LED}}\frac{\mathrm{d}A^{LED}}{\mathrm{d}U}$ are compared. The response A^{LED} at the same bias voltage is used in both cases to calculate them. The mean relative difference between the results with mounted and bare SiPMs is $-14\,\%$. This difference is expected, because the temperature difference between the two setups is approximately $3-5\,°\mathrm{C}$ and the relative voltage dependencies change with temperature, as explained in section 2.4. Thus, the results from the two setups are well consistent.

The voltage dependence of the SiPM response A^{MIP} to muons acting as MIPs in the cells of the AHCAL physics prototype is determined the same way [30]. The muon response is measured at different voltage settings at an average calorimeter temperature of 24 °C. The measurement procedure is explained in section 3.4. The mean $\frac{1}{A^{MIP}}\frac{\mathrm{d}A^{MIP}}{\mathrm{d}U}(MIP)$ is

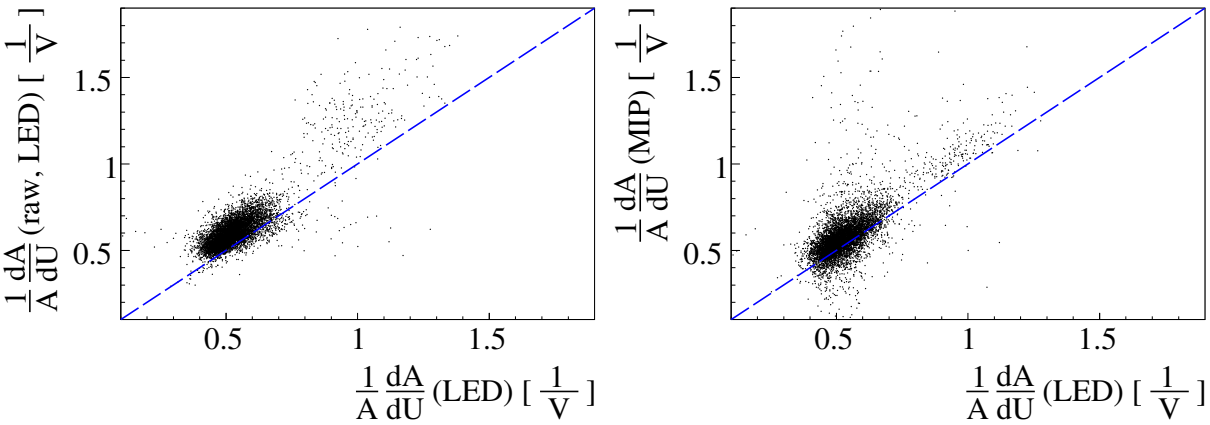

Figure 4.14: (left) The correlation between $\frac{1}{A}\frac{\mathrm{d}A}{\mathrm{d}U}$ determined for the bare SiPMs and for the SiPMs mounted on the tiles. Both results are obtained using LED light. Light intensities, temperatures, and data acquisition systems are different for the two measurements. (right) The correlation between $\frac{1}{A}\frac{\mathrm{d}A}{\mathrm{d}U}$ determined using LED light and scintillation light generated by MIPs passing through the tiles. Both measurements are performed with the fully assembled HCAL physics prototype, but at different temperatures. In both figures, the dashed lines indicate the one to one correspondences.

$5.6\,\frac{\%}{100\mathrm{mV}}$ with a spread of $0.8\,\frac{\%}{100\mathrm{mV}}$ (14 %) between the single AHCAL cells.

The correlation between the results for the relative voltage dependencies of the SiPM responses to LED light and to scintillation light generated by muons, both determined using the fully assembled AHCAL physics prototype, is only 58 % and is displayed in figure 4.14 (right). The σ_{90} of the difference between these values is $0.6\,\frac{\%}{100\mathrm{mV}}$, or 11 %. This is an estimate of the systematic uncertainty of the obtained voltage dependencies, although the responses A are generated differently for both measurement sets. Taking into account this uncertainty, the mean $\frac{1}{A^{MIP}}\frac{\mathrm{d}A^{MIP}}{\mathrm{d}U}$ of $5.6\,\frac{\%}{100\mathrm{mV}}$ agrees with the value of $7\,\frac{\%}{100\mathrm{mV}}$ quoted in [11] within 2 σ.

4.2.5 Temperature Dependence of the Response

The temperature dependence of the responses A^{MIP} of the SiPMs to muons are obtained analogue to the corresponding voltage dependence in section 4.2.4. For each cell, a linear fit is performed on several measurements of A^{MIP} done at the same operation voltage, but at different temperatures [30]. The average temperature is 27 °C. The mean extracted dependence $\frac{1}{A^{MIP}}\frac{\mathrm{d}A^{MIP}}{\mathrm{d}T}$ is $-3.7\,\frac{\%}{\mathrm{K}}$ with a spread of $1.1\,\frac{\%}{\mathrm{K}}$ between individual cells.

Since these are the only data this temperature dependence can be extracted from, a deduction of the systematic uncertainty from two independent measurements is not possible. Assuming the relative uncertainty to be 11 % as for the determination of the corresponding voltage dependencies, the result for the temperature dependence of the response matches the value of $-4.5\,\frac{\%}{100\mathrm{mV}}$ quoted in [11] within 2 σ.

dependence	mean (all cells)	error (single cell)	spread (all cells)	previous result
$\frac{1}{G}\frac{\mathrm{d}G}{\mathrm{d}U}$	$2.6\,\frac{\%}{100\mathrm{mV}}$	$0.1\,\frac{\%}{100\mathrm{mV}}$	$0.3\,\frac{\%}{100\mathrm{mV}}$	$2.5\,\frac{\%}{100\mathrm{mV}}$
$\frac{1}{G}\frac{\mathrm{d}G}{\mathrm{d}T}$	$-1.7\,\frac{\%}{\mathrm{K}}$	$0.2\,\frac{\%}{\mathrm{K}}$	$0.3\,\frac{\%}{\mathrm{K}}$	$-1.7\,\frac{\%}{\mathrm{K}}$
$\frac{1}{A}\frac{\mathrm{d}A}{\mathrm{d}U}$	$5.6\,\frac{\%}{100\mathrm{mV}}$	$0.6\,\frac{\%}{100\mathrm{mV}}$	$0.8\,\frac{\%}{100\mathrm{mV}}$	$7\,\frac{\%}{100\mathrm{mV}}$
$\frac{1}{A}\frac{\mathrm{d}A}{\mathrm{d}T}$	$-3.7\,\frac{\%}{\mathrm{K}}$	—	$1.1\,\frac{\%}{\mathrm{K}}$	$-4.5\,\frac{\%}{\mathrm{K}}$
$\frac{\mathrm{d}U_{bd}}{\mathrm{d}T}$	$65\,\frac{\mathrm{mV}}{\mathrm{K}}$	$9\,\frac{\mathrm{mV}}{\mathrm{K}}$	$11\,\frac{\mathrm{mV}}{\mathrm{K}}$	—

Table 4.1: Summary of the mean voltage and temperature dependencies of the gain and the response and the temperature dependence of the breakdown voltage of the SiPMs used in the AHCAL physics prototype. Results from previous measurements are quoted for comparison [11].

4.2.6 Summary of the Voltage and Temperature Dependencies

Table 4.1 summarises the mean voltage and temperature dependencies of the gain G and the response A^{MIP} to muon signals obtained for the AHCAL SiPM sample. For applications, the individual results for each SiPM are used instead of the means. The quoted error is the systematic uncertainty on the determination of each dependency. It is deduced from the comparison of two independent measurements of the same parameter. The spread corresponds to the variation of the parameters within the studied SiPM sample. The mean results are consistent with previous measurements [11]. The outcomes from these previous measurements are given in the last column of table 4.1.

As explained in section 2.4, the absolute voltage and temperature dependencies of G and A^{MIP} are, in contrast to the relative values, device specific constants and do not change with operation voltage and temperature. Thus, the absolute dependencies are used for the applications described in chapter 5.

Chapter 5

Adjustment of Calibration Parameters

The AHCAL physics prototype described in section 3 comprises 7608 SiPMs mounted on plastic scintillator tiles. Calibrating this detector requires knowing two coefficients for each individual SiPM: the gain G and the response A^{MIP} to muons depositing energy in the corresponding tile (see section 3.6). Since these SiPM parameters change with operation voltage U_{bias} and temperature T (see section 2.4), they are only valid for energy measurements performed under the same operation conditions as the calibration measurements. The dependencies of the gain and the muon response of the SiPMs of the AHCAL physics prototype on temperature and voltage are obtained in in chapter 4. As mentioned in that chapter, monitoring variations of voltage and temperature and calculating their impact on the calibration coefficients is an alternative to measuring these coefficients repeatedly.

In this chapter, an approach to improve the calibration on the centigrade scale of the temperature sensors used in the AHCAL physics prototype is explained and the temperature profile inside this calorimeter is studied. The effect of a fan-based cooling system on the temperature profile is illustrated.

Methods are presented which either aim for correcting the calibration coefficients G and A^{MIP} for the effects of changes in temperature or for compensating these effects via adjusting the bias voltages of the SiPMs. The systematic uncertainties introduced by these procedures are quantified.

The light yield of the cells of the AHCAL physics prototype is a measure of the detector performance (see section 3.5). A procedure to adjust the light yield via voltage adjustments is applied and the results are discussed.

As in chapter 4, the ROOT analysis framework (version 5.16) [28] is used for the studies described in this chapter and the standard deviation of the centre 90 % of the normally distributed entries of a histogram is called σ_{90}.

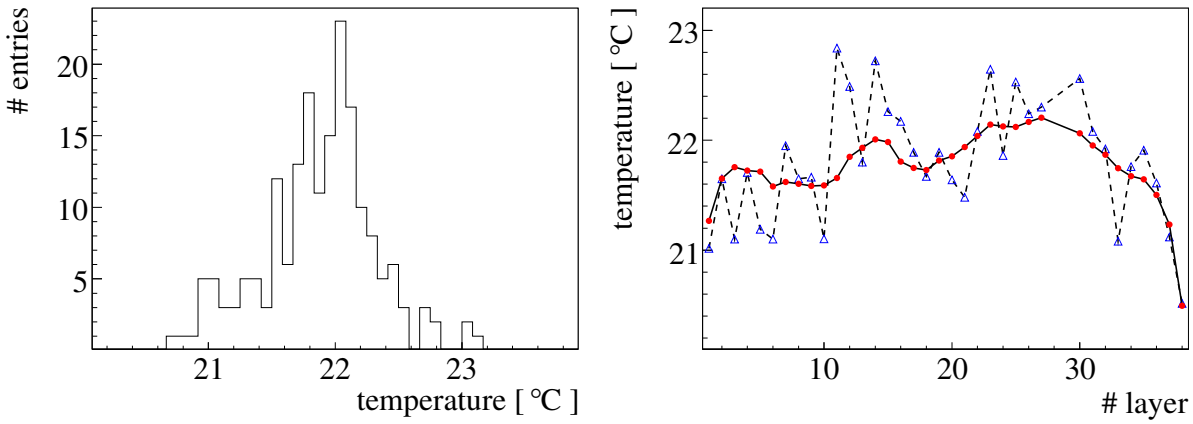

Figure 5.1: (left) All temperature sensor readings from a single measurement. (right) Longitudinal temperature profile with sensor calibration (dots) and without (triangles).

5.1 Temperature Sensor Calibration

As described in section 3.1, the monitoring system of the AHCAL physics prototype comprises five temperature sensors inside the module cassettes. The sensors in modules 1 and 2 are placed in a diagonal line from the top left to the bottom right corner of the cassettes, while the sensors in the other modules are positioned along a vertical line in the centres of the cassettes. Counting from top to bottom, the sensors in each module are numbered from 1 to 5.

The temperature sensors used for the prototype measure absolute temperatures with an uncertainty of 0.5 °C [31], i.e. each sensor has an offset on the centigrade scale and the distribution of the offsets of the whole sensor sample has a mean of zero and a width of 0.5 °C. In order to improve the calibration of each individual sensor, their offsets can be determined and added to the readings. The temperature in the prototype has to be at equilibrium, which can be achieved by leaving the system off for a long time. Under this condition, each temperature sensor is assumed to measure the same temperature. The mean of all sensor readings is the real temperature throughout all layers, without any offset. The Result from a temperature measurement performed in this state is presented in figure 5.1 (left).

The calibration offset C_i for each temperature sensor is obtained as the difference between its reading T_i from the average $\bar{T}$ of all sensors,

$$C_i = \bar{T} - T_i \; . \tag{5.1}$$

This procedure yields a calibration offset for 187 out of 190 sensors. The offsets C_i applied in the following are the average of 50 consecutive calibration offset measurements. Figure 5.1 (right) displays the temperature values from the centre sensors of all layers. The triangles represent the values before and the dots those after adding the calibration offsets C_i. Since the AHCAL physics prototype mainly is a solid steel structure, one expects

a steady longitudinal temperature profile without strong fluctuations from layer to layer. However, the profile measured without the sensor calibration does not meet this expectation. Only after adding the calibration offsets C_i the profile looks reasonably smooth. Usually the temperature varies by at least 2 °C along the calorimeter. This implies that a mean temperature can only be used as a rough estimate, but is not convenient for studying temperature effects of the order of $\frac{\%}{K}$.

Sometimes single temperatures are missing, either because a sensor malfunctions or a readout problem occurs. As long as this only affects single sensors, the corresponding temperatures can be obtained by linearly interpolating the values measured by the sensors of the adjacent layers at the same positions. This interpolation is only possible after sensor calibration.

5.2 Temperature Profiles

Figure 5.2 (left) shows two longitudinal temperature profiles in the AHCAL physics prototype measured at the same environmental temperature. In both cases the values presented are the ones measured by the middle sensor of each layer. The calibration described in section 5.1 is applied. The only difference between the two temperature measurements is an improvement in the cooling of the VFE electronics and the CMB boards. Both the housings of the VFE electronics and the CMBs are closed. Tubes are connected to the top and to the bottom part of the housings. The tubes lead compressed air into the housings. The air streams along the electronics inside and leaves through open gaps. For the improvement of the cooling, additional fans are placed in front of the CMBs and on top of and below the VFE electronics housings. These fans create an additional air stream between the electronics housings of the different modules. Due to this fan-based improvement of the cooling, the average calorimeter temperature decreases from 27 °C to 22 °C and the layer to layer temperature variation from 5 °C to less than 2 °C. This illustrates the usefullness of the additional fans.

In figure 5.2 (right), two examples of temperature profiles within single modules are presented. The dots show the values measured by the five sensors of module 24 in layer 30, which are distributed in a line from top to bottom. The triangles are the readings from the sensors of module 2 in layer 29, which lie on a diagonal line across the module. The two modules are positioned next to each other in the prototype. The figure shows that the temperature from top to bottom varies by less than 0.5 °C within one module, while along the diagonal axis it changes by 1 °C. From this one can conclude that the horizontal profile is not flat either. The temperature at the VFE electronics side of the modules appears to be higher than at the CMB side. This is confirmed by comparing the readings from the temperature sensors in the VFE electronics and the CMBs.

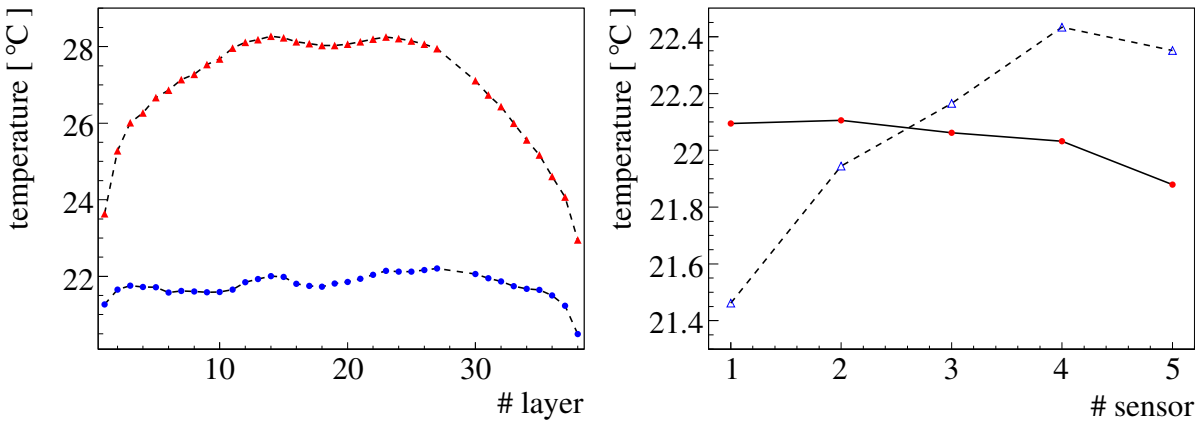

Figure 5.2: (left) Longitudinal temperature profile with fan-based cooling (dots) and without (triangles). (right) Profile along the vertical (dots, module 24) and the diagonal module axis (triangles, module 2).

5.3 Temperature Correction and Voltage Adjustment

5.3.1 Gain Scaling using Temperature Measurements

The temperature dependencies of the gains of the SiPMs used in the AHCAL physics prototype are determined in section 4.2.2. Using them, it is possible to correct the gains for temperature variations offline. The relative difference between the results of two gain measurements performed with the AHCAL physics prototype under the same conditions, i.e. at the same operation voltages and temperature, is shown in figure 5.3. The σ_{90} is 0.7 %. This quantifies the relative uncertainity of a gain determination.

To test the temperature correction procedure, two sets of gain measurements G_1 and

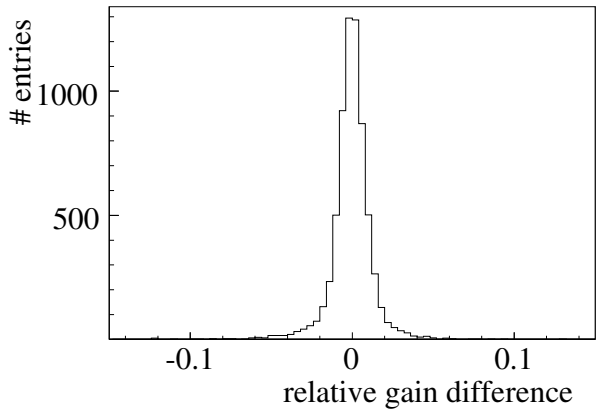

Figure 5.3: Relative difference between two gain measurements performed under the same conditions. The σ_{90} of this distribution is 0.7 %.

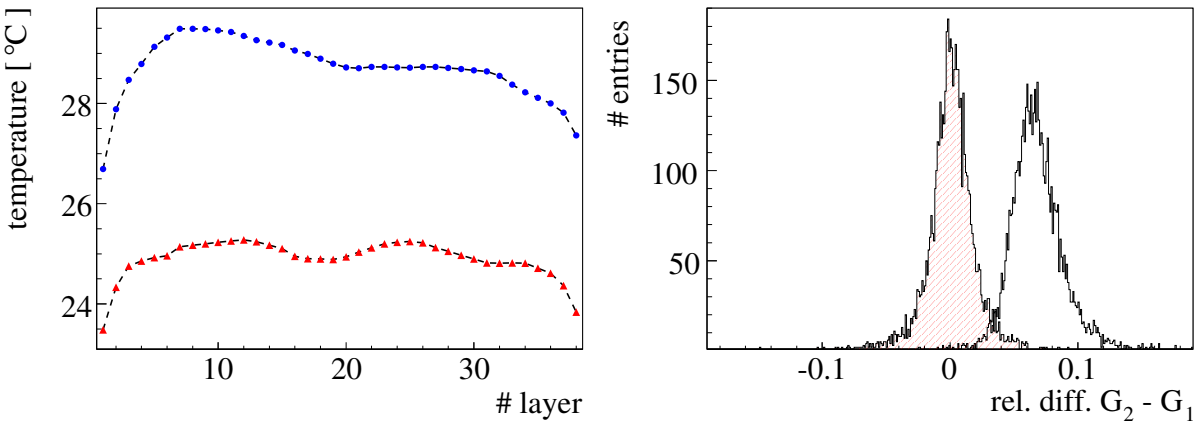

Figure 5.4: (left) Temperatures of the centre sensors of all layers during the measurement of $G_1(T_1)$ (dots) and $G_2(T_2)$ (triangles). (right) Relative difference between G_1 and G_2 without (open histogram) and with applied temperature correction (shaded histogram).

G_2 obtained at different average calorimeter temperatures $\bar{T}_1 = 28.7\,°\mathrm{C}$ and $\bar{T}_2 = 24.9\,°\mathrm{C}$ are compared. The temperature readings from the centre sensors of all layers during these measurements are displayed in figure 5.4 (left). The open histogram in figure 5.4 (right) shows the relative difference between $G_2(\overline{T_2})$ and $G_1(\overline{T_1})$. The mean difference is 6.6 %, the σ_{90} is 1.5 %. The uncertainty is larger than the uncertainty observed when comparing two gain measurements done under the same conditions. There are two contributions to the increased width. First, the temperature dependence of the gains of the SiPMs varies within the sample and the same temperature change results in different gain changes. Second, the shape of the temperature profile differs between the two measurement sets. Thus, the temperature changes and the resulting gain variatons are different for SiPMs in different parts of the detector.

Using the slopes $\frac{\mathrm{d}G}{\mathrm{d}T}$, which are determined independently from the measurements G_1 and G_2, the values G_2 are shifted to the temperature T_1 applying

$$G_2^i(T_1^i) = G_2^i(T_2^i) + \left(\frac{\mathrm{d}G}{\mathrm{d}T}\right)^i \cdot (T_1^i - T_2^i)\,. \tag{5.2}$$

The correction is done for each SiPM individually, where i is the SiPM index. The relative difference between $G_2(\overline{T_1})$ and $G_1(\overline{T_1})$ is presented by the shaded histogram in figure 5.4 (right). The mean difference is successfully reduced zero with a σ_{90} of 1.3 %, which is the relative uncertainty of the corrected gains.

Starting from equation 5.2, the contributions of different errors to the relative uncertainty of the corrected $G_2(T_1)$, $\frac{\sigma^c_{G_2}}{\overline{G}}$, is given by

$$\left(\frac{1}{\overline{G}}\right)^2 \left(\sigma_{G_2^c}\right)^2 = \left(\frac{1}{\overline{G}}\right)^2 (\sigma_{G_2})^2 + \left(\frac{1}{\overline{G}}\frac{\mathrm{d}G}{\mathrm{d}T}\right)^2 (\sigma_{\Delta T})^2 + (\Delta T)^2 \left(\sigma_{\frac{1}{\overline{G}}\frac{\mathrm{d}G}{\mathrm{d}T}}\right)^2\,, \tag{5.3}$$

where $\overline{G}$ is the average gain, i.e. $2\frac{G_2-G_2^c}{G_2+G_2^c}$. Inserting the uncertainty of a single gain measurement for $\frac{\sigma_{G_2}}{\overline{G}}$, the value and the systematic error obtained for $\frac{1}{\overline{G}}\frac{\mathrm{d}G}{\mathrm{d}T}$ in section 4.2.2 and the average temperature difference $\Delta T = T_1 - T_2$ of 3.8 °C allows for calculating the uncertainty of the temperature difference, $\sigma_{\Delta T}$. It turns out to be $\approx 0.5\,\mathrm{K}$, which is of the same order as the precision quoted for the temperature sensors by the producer [31]. Changes in the temperature profile, which are not detected due to the limited number of temperature sensors, contribute to $\sigma_{\Delta T}$ as well.

5.3.2 MIP Response Scaling using Temperature Measurements

The response signals A of the SiPMs used in the AHCAL physics prototype can be corrected offline for temperature changes as well. The correction procedure is analogue to the one described for the gain in section 5.3.1. The relative difference between two measurements of A^{MIP} done at the same operation voltages, but at different temperatures, is presented by the open histogram in figure 5.5 (right). The first measurement set, A_1^{MIP}, is performed at an average calorimeter temperature of $\overline{T_1} = 21.9\,^{\circ}\mathrm{C}$. The data from the second set, A_2^{MIP}, are collected at $\overline{T_2} = 24.0\,^{\circ}\mathrm{C}$. The mean difference between the results from the two measurements is $-8.2\,\%$.

The temperature dependence of the MIP responses from section 4.2.5 and equation 5.2 allow for shifting the second measurement to $\overline{T_1}$. The responses A_1^{MIP} and A_2^{MIP} replace the gains G_1 and G_2 in the applied equation. The shaded histogram in figure 5.5 (right) shows the relative difference between $A_1^{MIP}(\overline{T_1})$ and $A_2^{MIP}(\overline{T_1})$. The mean is at $-0.7\,\%$, the σ_{90} is $2.7\,\%$. The deviation of the mean from zero indicates that the applied correction is too small. The measurements of A^{MIP} take several hours, during which the temperature changes by approximately 0.3 °C, while the temperatures used for the correction are averaged over the whole measurement time. According to the results from section 4.2.5, a temperature change of 0.3 °C leads to an average A^{MIP} shift of $1.2\,\%$. This explains the remaining offset after the correction.

The relative uncertainty $\frac{\sigma_{A^{MIP}}}{A^{MIP}}$ of single determinations of A^{MIP} depends on the number of events collected during the corresponding measurements. Judging from muon calibration sets with approximately 2 million events, a lower limit for this uncertainty is $1.5\,\%$ [26].

The error $\sigma_{\frac{1}{A}\frac{\mathrm{d}A}{\mathrm{d}T}}$ of the extracted temperature dependence of A^{MIP} can not be deduced from independent measurements (see section 4.2.5). By replacing the gain related values in equation 5.3 with the corresponding values for A^{MIP}, this error can be estimated. Inserting the known factors, including the lower limit for $\frac{\sigma_{A^{MIP}}}{A^{MIP}}$ of $1.5\,\%$ and the $\sigma_{\Delta T}$ obtained in section 5.3.1, leads to $\sigma_{\frac{1}{A^{MIP}}\frac{\mathrm{d}A^{MIP}}{\mathrm{d}T}} < 0.6\,\frac{\%}{100\mathrm{mV}}$. This outcome is comparable to the error of the MIP voltage dependencies quoted in section 4.2.4.

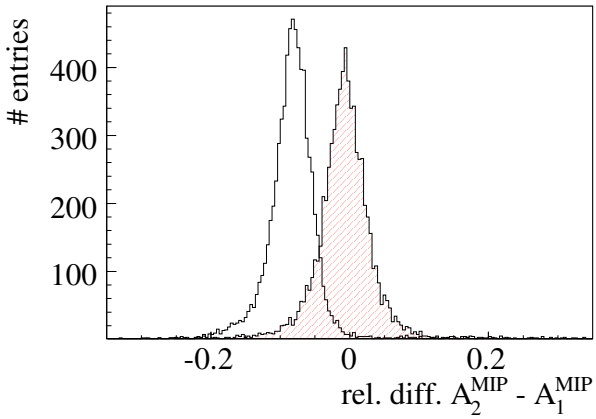

Figure 5.5: Comparison between two A^{MIP} measurements done at the same voltage settings, but at different temperatures. The relative differences between the measurements without temperature correction (open histogram) and after applying the correction (shaded histogram) are shown.

5.3.3 Gain Stabilisation via Voltage Adjustment

Gain changes caused by temperature variations can be compensated by adjusting the bias voltage of a photodetector in Geiger mode. Choosing the proper bias voltage U_2 shifts a gain value G_2 measured at this voltage and at a temperature $T = T_2$ to the gain value G_1, which is valid at a different temperature $T = T_1$ and at $U_{bias} = U_1$, i.e.

$$G_2(U_2, T_2) = G_1(U_1, T_1) \; . \tag{5.4}$$

The sketch in figure 5.6 (left) visualises this. The voltage U_2 needed to make the gain $G_2(U, T_2)$ equal $G_1(U_1, T_1)$ can be calculated using either

$$U_2 = U_1 - \frac{\mathrm{d}U_{bd}}{\mathrm{d}T} \cdot (T_1 - T_2) \tag{5.5}$$

or

$$U_2 = U_1 + \frac{G_1 - G_2}{\frac{\mathrm{d}G}{\mathrm{d}U}} \; , \tag{5.6}$$

where $\frac{\mathrm{d}U_{bd}}{\mathrm{d}T}$ is the temperature dependence of the breakdown voltage (see section 4.2.3). The voltage adjustment also shifts the photon detection efficiency from $\varepsilon_2(U_1, T_2)$ to $\varepsilon_1(U_1, T_1)$.

To verify this procedure using the SiPMs in fully assembled AHCAL physics prototype, the gain G_{pred} after a voltage change of ΔU is predicted:

$$G^i_{pred} = G^i_{meas} + (\frac{dG}{dU})^i \cdot \Delta U^i \tag{5.7}$$

The initial gain G^i_{meas} is measured for each SiPM i. In this example, all bias voltages are increased by 0.2 V. The gain voltage dependencies determined at 27 °C (see section

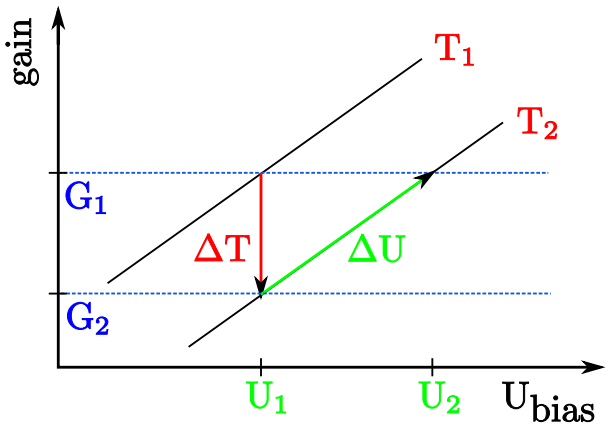

Figure 5.6: Sketch of the general idea of voltage adjustment. A change of gain due to temperature effects can be compensated by modifying the bias voltage appropriately.

4.2.1) are used. The open histogram in figure 5.7 presents the relative differences between G_{pred} and G_{meas}. The mean difference is 4.8 %. A second gain measurement is done after applying the chosen ΔU to the system. The relative difference between the results of this second measurement, G^{adj}_{meas}, and the prediction G_{pred} is displayed by the shaded histogram in figure 5.7. The mean is at zero. The σ_{90} of 1 % is the uncertainty $\frac{\sigma_{G_{pred}}}{\overline{G}}$ of the predicted gain, where $\overline{G} = 2\frac{G_{pred}-G_{meas}}{G_{pred}+G_{meas}}$. This uncertainty is larger than the gain measurement uncertainty $\frac{\sigma_{G_{meas}}}{\overline{G}}$ of 0.7 % (see section 5.3.1). The increase is caused by the error of the applied slopes, $\sigma_{\frac{1}{\overline{G}}\frac{\mathrm{d}G}{\mathrm{d}T}}$, and the error on the voltage settings, $\sigma_{\Delta U}$:

$$\left(\frac{1}{\overline{G}}\right)^2 \left(\sigma_{G_{pred}}\right)^2 = \left(\frac{1}{\overline{G}}\right)^2 \left(\sigma_{G_{meas}}\right)^2 + \left(\frac{1}{\overline{G}}\frac{\mathrm{d}G}{\mathrm{d}U}\right)^2 \left(\sigma_{\Delta U}\right)^2 + (\Delta U)^2 \left(\sigma_{\frac{1}{\overline{G}}\frac{\mathrm{d}G}{\mathrm{d}U}}\right)^2 . \tag{5.8}$$

Inserting all known parameters yields $\sigma_{\Delta U} = 27\,\mathrm{mV}$. This matches the error quoted by the producer for the output of the high voltage power supplies [32].

5.3.4 MIP Response Stabilisation via Voltage Adjustment

Not only the gain of a photodetector operated in Geiger mode, but also its response is shifted by changing the bias voltage. As for the gain, a proper voltage adjustment compensates the effects of temperature changes on the response. The procedure is the same as explained for the gain in section 5.3.3. The voltage adjustment $U_2 - U_1$ needed to compensate a certain temperature difference $(T_1 - T_2)$ is the same as for the gain. In addition to equations 5.5 and 5.6 , the needed adjustment can also be determined by replacing G_1, G_2 and $\frac{\mathrm{d}G}{\mathrm{d}U}$ in equation 5.6 with A_1, A_2 and $\frac{\mathrm{d}A}{\mathrm{d}U}$.

In order to test the option of stabilising the responses of the SiPMs to muons via voltage adjustment, an initial measurement A^{MIP}_{meas} is performed. Analogue to equation 5.7,

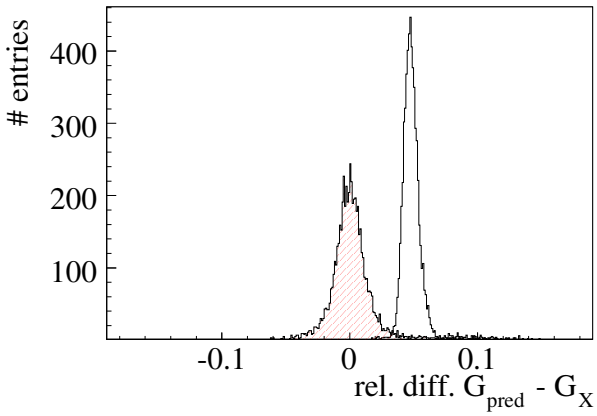

Figure 5.7: Relative difference between the predicted gain after voltage adjustment, G_{pred}, and the measured gain ($G_X = G_{meas}$, open histogram) and the relative difference between the predicted gain G_{pred} and the measured gain after applying the voltage adjustments ($G_X = G^{adj}_{meas}$, shaded histogram).

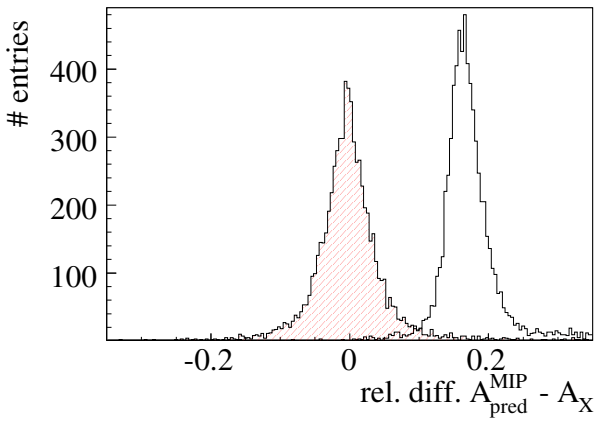

Figure 5.8: Relative difference between the predicted response of the cells of the AHCAL physics prototype to muons after voltage adjustment, A^{MIP}_{pred}, and the measured response ($A_X = A^{MIP}_{meas}$, open histogram) and the relative difference between the predicted result A^{MIP}_{pred} and the measured response after applying the voltage adjustments ($A_X = A^{MIP,adj}_{meas}$, shaded histogram).

the response A_{pred}^{MIP} after a voltage increase of $\Delta U = +300\,\mathrm{mV}$ is predicted. The open histogram in figure 5.8 shows the relative difference between A_{meas}^{MIP} and A_{pred}^{MIP}. The mean difference is 17 %, which is expected due to the difference in voltage. The voltage shift ΔU is applied to the AHCAL physics prototype and the responses of the cells to muons are measured again, yielding $A_{meas}^{MIP,adj}$. The shaded histogram in figure 5.8 shows the relative difference between the results from this second measurement and the prediction. The mean is at zero, the σ_{90} is 3.2 %. As explained for the error of the predicted gains in section 5.3.3, the errors of the voltage dependencies of the responses and the errors of the voltage settings contribute to this error. Replacing the gain related factors in equation 5.8 by the corresponding values for the MIP response, including the estimate $\frac{\sigma_{A^{MIP}}}{A^{MIP}} > 1.5\,\%$ (see section 5.3.2), leads to a voltage error of $\sigma_{\Delta U} < 40\,\mathrm{mV}$. This agrees with the result extracted in section 5.3.3.

5.3.5 MIP Response Scaling using Gain Measurements

Knowing a direct relation between changes of the gain G and changes of the photon detection efficiency ε or the response signal A of a photodetector in Geiger mode provides a new monitoring and correction possibility. Determining ε or A repeatedly can be replaced by calculating the shifts of these parameters from measured gain variations. While directly measuring the photon detection efficiency or the response requires quantifying the intensity of the light source used, this intensity is not needed to acquire the gain. Having to measure one parameter less makes the monitoring procedure easier. Monitoring the gain summarises the information of voltage and temperature for each individual SiPM, so that correcting for gain changes corrects both for temperature and voltage changes. A drawback of this procedure is that gain measurements are much more time consuming than voltage or temperature measurements. For the AHCAL physics prototype, for example, determining the gain of all included SiPMs takes more than an hour.

Relation between Changes of the MIP Response and the Gain

In order to obtain a relation between gain and response variations, one can formally write:

$$\frac{\mathrm{d}A}{\mathrm{d}U} \cdot \frac{\mathrm{d}U}{\mathrm{d}G} = \left.\frac{\mathrm{d}A}{\mathrm{d}G}\right|_U \tag{5.9}$$

$$\frac{\mathrm{d}A}{\mathrm{d}T} \cdot \frac{\mathrm{d}T}{\mathrm{d}G} = \left.\frac{\mathrm{d}A}{\mathrm{d}G}\right|_T \tag{5.10}$$

Assuming that the number of incoming photons is fixed, one expects the ratios in equation (5.9) and (5.10) to yield the same result. Figure 5.9 shows the correlation between these ratios determined using the results from the first measurement sets of $\frac{\mathrm{d}G}{\mathrm{d}U}$ and $\frac{\mathrm{d}G}{\mathrm{d}T}$ described in sections 4.2.1 and 4.2.2. For $\frac{\mathrm{d}A}{\mathrm{d}U}$ and $\frac{\mathrm{d}A}{\mathrm{d}T}$ results from the muon response measurements are used (see sections 4.2.4 and 4.2.5). The correlation is only 34 %. The mean relative difference between $\left.\frac{\mathrm{d}A}{\mathrm{d}G}\right|_U$ and $\left.\frac{\mathrm{d}A}{\mathrm{d}G}\right|_T$ is 5 %, with a large σ_{90} of 27 %.

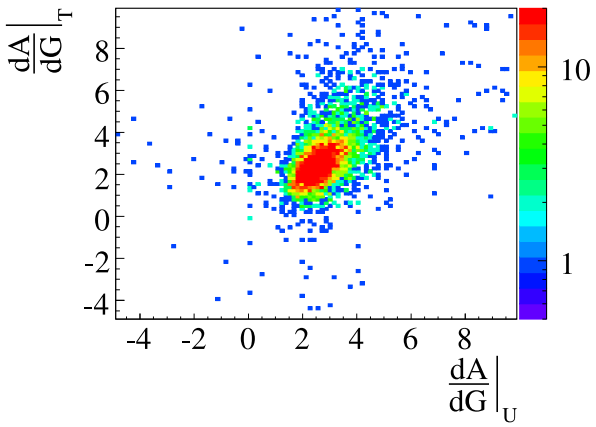

Figure 5.9: Correlation between $\frac{\mathrm{d}A}{\mathrm{d}G}$ determined from the voltage dependencies ($\frac{\mathrm{d}A}{\mathrm{d}G}|_U$) and from the temperature dependencies ($\frac{\mathrm{d}A}{\mathrm{d}G}|_T$) of A and G.

Application of the Gain Correction Procedure

The relative difference between two muon response measurements A_1^{MIP} and A_2^{MIP} performed with the AHCAL physics prototype at the same voltage settings, but at different temperatures, is presented by the open histogram in figure 5.10. The measurements are the same as used in section 5.3.2. The gain G_1 is the mean of 3 gain measurements done during obtaining A_1^{MIP}, G_2 is the mean of 2 gain measurements done close to the measurement of A_2^{MIP}. Analogue to equation 5.2 on page 51, shifting $A_2^{MIP}(G_2)$ to the operation conditions of $A_1^{MIP}(G_1)$ is performed by calculating

$$A_2^{MIP}(G_1) = A_2^{MIP}(G_2) + (\frac{dA}{dG}) \cdot (G_1 - G_2) \; . \tag{5.11}$$

The shaded histogram in figure 5.10 shows the relative difference between A_1^{MIP} and A_2^{MIP} after shifting A_2^{MIP} to G_1 using $\frac{\mathrm{d}A}{\mathrm{d}G}|_U$. The mean difference is 2 % with a σ_{90} of 3 %. The gain adjustment overcorrects the temperature differences between $A_1^{MIP}(G_1)$ and $A_2^{MIP}(G_2)$ by 2 %. As mentioned in section 5.3.2, the measurements of A^{MIP} take several hours. The average temperatures $\overline{T_1}$ and $\overline{T_2}$ during the A^{MIP} measurements are 21.9 °C and 24.0 °C. The average temperatures during the gain measurements G_1 and G_2 are 21.7 °C and 26.0 °C. The discrepancy of 2 °C between the average temperature of the second set of muon responses and the second set of gain measurements corresponds to a gain deviation of approximately 3 %, which is of the same order as the observed overcorrection.

The uncertainty on the MIP amplitudes after gain correction is of the same order as after the temperature correction described in section 5.3.2. The large uncertainty on the $\frac{\mathrm{d}A}{\mathrm{d}G}$ values cancels the advantage of the individual status informations for each SiPM which are used for this method. Considering the temperature information in the AHCAL physics prototype are recorded along with any other measurement and are thus known at each time, the correction using temperature measurements is the method to prefer. However, if

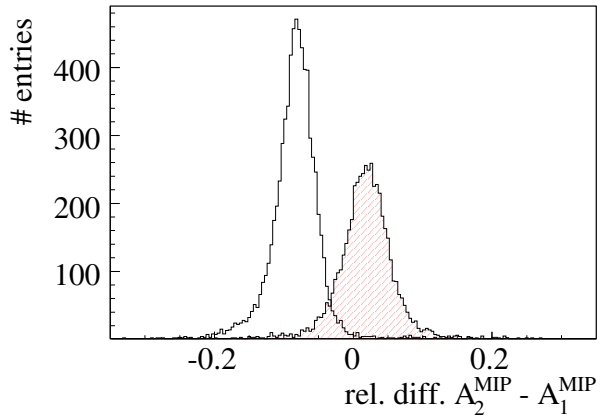

Figure 5.10: Relative difference between two measurements of A^{MIP} performed at different temperatures without (open histogram) and with gain correction (shaded histogram).

the uncertainty on the $\frac{dA}{dG}$ values can be reduced by further measurements, the correction using gain measurements is expected to be the more accurate procedure.

5.3.6 Summary of Correction and Adjustment Procedures

The previous sections demonsrate the successful application of procedures to predict the effect of bias voltage adjustments and to correct for the impact of temperature changes on both the gain and the muon response of the SiPMs used in the AHCAL physics prototype. Table 5.1 summarises these procedures and the uncertainties they add to the measurement precisions. The effects of voltage or temperature changes on the parameter X, which is either the gain G or the MIP response A^{MIP}, are quoted in the second column. The third column gives the relative error $\frac{\sigma_0}{X}$ on a measurement of X. The third column contains a constant uncertainty $\frac{\sigma_{const}}{X}$ which is caused by the uncertainty on the output voltage of the voltage power supplies or the temperature measurement. The term in the last column, $\frac{\sigma_{lin}}{X}$, corresponds to the error of the applied dependencies and increases linearly with the amount of temperature correction or voltage shift. The total relative uncertainty after calculating the value of X at operation conditions differing from the measurement conditions is

$$\frac{\sigma_X}{X} = \sqrt{\left(\frac{\sigma_0}{X}\right)^2 + \left(\frac{\sigma_{const}}{X}\right)^2 + \left(\frac{\sigma_{lin}}{X}\right)^2}\,. \tag{5.12}$$

In principle, the correction of A^{MIP} using gain measurements is an alternative to the correction procedure using temperature measurements. But given the large uncertainty of the determined $\frac{dA^{MIP}}{dG}$ relations, their application yields no advantage over using the more precisely known $\frac{dA^{MIP}}{dT}$ dependencies.

	effect	$\frac{\sigma_0}{X}$	$\frac{\sigma_{const}}{X}$	$\frac{\sigma_{lin}}{X}$
$G(U,T) \rightarrow G(U,T+\Delta T)$	$-1.7\,\frac{\%}{\mathrm{K}}$	$0.7\,\%$	$0.9\,\%$	$0.2\,\frac{\%}{\mathrm{K}} \cdot \Delta T$
$A^{MIP}(U,T) \rightarrow A^{MIP}(U,T+\Delta T)$	$-3.7\,\frac{\%}{\mathrm{K}}$	$> 1.5\,\%$	$1.9\,\%$	$< 0.6\,\frac{\%}{\mathrm{K}} \cdot \Delta T$
$G(U,T) \rightarrow G(U+\Delta U,T)$	$2.6\,\frac{\%}{100\mathrm{mV}}$	$0.7\,\%$	$0.8\,\%$	$0.1\,\frac{\%}{100\mathrm{mV}} \cdot \Delta U$
$A^{MIP}(U,T) \rightarrow A^{MIP}(U+\Delta U,T)$	$5.6\,\frac{\%}{100\mathrm{mV}}$	$> 1.5\,\%$	$< 2.2\,\%$	$0.6\,\frac{\%}{100\mathrm{mV}} \cdot \Delta U$

Table 5.1: Summary of the procedures correcting for or compensating the effects of temperature changes on the gains G and the responses A^{MIP} to muons of the SiPMs in the AHCAL physics prototype and the uncertainties introduced the application of these procedures.

5.4 Light Yield Scaling via Voltage Adjustment

As mentioned in section 3.5, the light yield of the AHCAL physics prototype cells is a measure of the detector performance. If the operation temperature changes, the SiPM bias voltages need to be re-adjusted to keep the light yield at a fixed value. Assuming that the light yield is the same under different operation conditions if the gain is, the required voltage adjustments can be calculated using the results from the previous sections. In addition, the voltage adjustment needed to shift the light yield to a different value can be calculated. The adjustment procedure and the result of its application are described in the following sections.

5.4.1 Voltage Dependence of the Light Yield

The light yield LY of a combined system of SiPM and scintillator tile is proportional to the photon-detection efficiency ε of the SiPM. As a result, the relative voltage dependence of the light yield is equal to the relative voltage dependence of the photon detection efficiency:

$$\frac{1}{LY} \cdot \frac{\mathrm{d}LY}{\mathrm{d}U} = \frac{1}{\varepsilon} \cdot \frac{\mathrm{d}\varepsilon}{\mathrm{d}U} \,. \tag{5.13}$$

Using equation 5.13, equation 2.8 and the light yield definition 3.5, the absolute light yield voltage dependence is

$$\frac{\mathrm{d}LY}{\mathrm{d}U} = \frac{A}{G \cdot IC_{cell}} \cdot \left(\frac{1}{A}\frac{\mathrm{d}A}{\mathrm{d}U} - \frac{1}{G}\frac{\mathrm{d}G}{\mathrm{d}U}\right) . \tag{5.14}$$

To apply this relation, A and G need to be given at the same bias voltages and temperatures. The intercalibration factor IC_{cell} is required as well. As described for $\frac{\mathrm{d}\varepsilon}{\mathrm{d}U}$ in section 2.4, the transition to an absolute relation $\frac{\mathrm{d}LY}{\mathrm{d}U}$ yields a dependence that is independent from the actual operation voltage and temperature.

The light yield voltage dependence is calculated using the results for A at nominal bias voltage and $\frac{\mathrm{d}A}{\mathrm{d}U}$ from the MIP measurements, both done at an average temperature of 24 °C. For G and $\frac{\mathrm{d}G}{\mathrm{d}U}$, results acquired at 25 °C are used. The same intercalibration factors as in section 4.1 are chosen. For the SiPMs studied, the mean value of $\frac{\mathrm{d}LY}{\mathrm{d}U}$ is $0.4\,\frac{\mathrm{pix}}{100\mathrm{mV}}$ with a spread of $0.1\,\frac{\mathrm{pix}}{100\mathrm{mV}}$ between the individual cells of the AHCAL prototype.

As explained in section 2.2, the increase in photon detection efficiency with bias voltage, and thus the light yield increase, saturates.

5.4.2 Application of the Light Yield Adjustment

The voltage adjustment ΔU shifting the light yield of the cells of the AHCAL physics prototype to a desired value LY_b is determined in two steps. A gain measurement G_1 is performed at given operation conditions (temperature T_1 and bias voltage U_1). The first voltage adjustment $(\Delta U)_G$ shifts G_1 to G_{LY} and is calculated using equation 5.6. The gain G_{LY} has to be the gain at operation conditions (temperature T_{LY} and and bias voltage U_{LY}) for which the light yield, LY_a, is known. This voltage adjustment also shifts the light yield from an unknown initial value to LY_a. The second voltage adjustment, $(\Delta_U)_{LY}$, changes the light yield from LY_a to LY_b. It is calculated according to

$$(\Delta U)_{LY} = \frac{LY_b - LY_a}{\frac{\mathrm{d}LY}{\mathrm{d}U}} \,. \tag{5.15}$$

The sum of $(\Delta U)_G$ and $(\Delta_U)_{LY}$ yields the total voltage adjustment ΔU required to achieve LY_b.

Starting from a gain measurement G_1 performed at an average calorimeter temperature of 24 °C, $(\Delta U)_G$ and $(\Delta_U)_{LY}$ are calculated. A light yield of $LY_b = 14\,\frac{\mathrm{pix}}{\mathrm{MIP}}$ is the aim of the adjustment. This value is $1\,\frac{\mathrm{pix}}{\mathrm{MIP}}$ lower than the defined optimum of $15\,\frac{\mathrm{pix}}{\mathrm{MIP}}$ to ensure that the tuned voltages do not get too large and damage the SiPMs. For convenience, the medians for each half module are determined and only discrete adjustment steps of $-0.3\,\mathrm{V}$, $+0.0\,\mathrm{V}$, $+0.3\,\mathrm{V}$ and $+0.5\,\mathrm{V}$ are allowed and assigned to the half modules according to the calculated medians.

Figure 5.11 (top left) shows the resulting light yields of all AHCAL cells after applying the determined voltage adjustment. The mean value is $13.3\,\frac{\mathrm{pix}}{\mathrm{MIP}}$ with a spread of $2.9\,\frac{\mathrm{pix}}{\mathrm{MIP}}$ between single cells. The other three histograms in figure 5.11 show the light yields of the cells with tiles of different size. The mean light yield of the 3 x 3 cm^2 tiles is $12.9\,\frac{\mathrm{pix}}{\mathrm{MIP}}$ with a spread of $2.9\,\frac{\mathrm{pix}}{\mathrm{MIP}}$, the mean of the 6 x 6 cm^2 tiles is $14.2\,\frac{\mathrm{pix}}{\mathrm{MIP}}$ with a spread of $2.7\,\frac{\mathrm{pix}}{\mathrm{MIP}}$ and the mean of the 12 x 12 cm^2 tiles is $10.8\,\frac{\mathrm{pix}}{\mathrm{MIP}}$ with a spread of $2.4\,\frac{\mathrm{pix}}{\mathrm{MIP}}$. The light yield of the 6 x 6 cm^2 cells matches the aim of $14\,\frac{\mathrm{pix}}{\mathrm{MIP}}$. The differences between the mean light yields of cells of different tile size are observed during other measurements as well, as described in section 3.7. Since the voltage adjustment is not done for each cell individually, this procedure does not compensate the light yield differences between cells of different size.

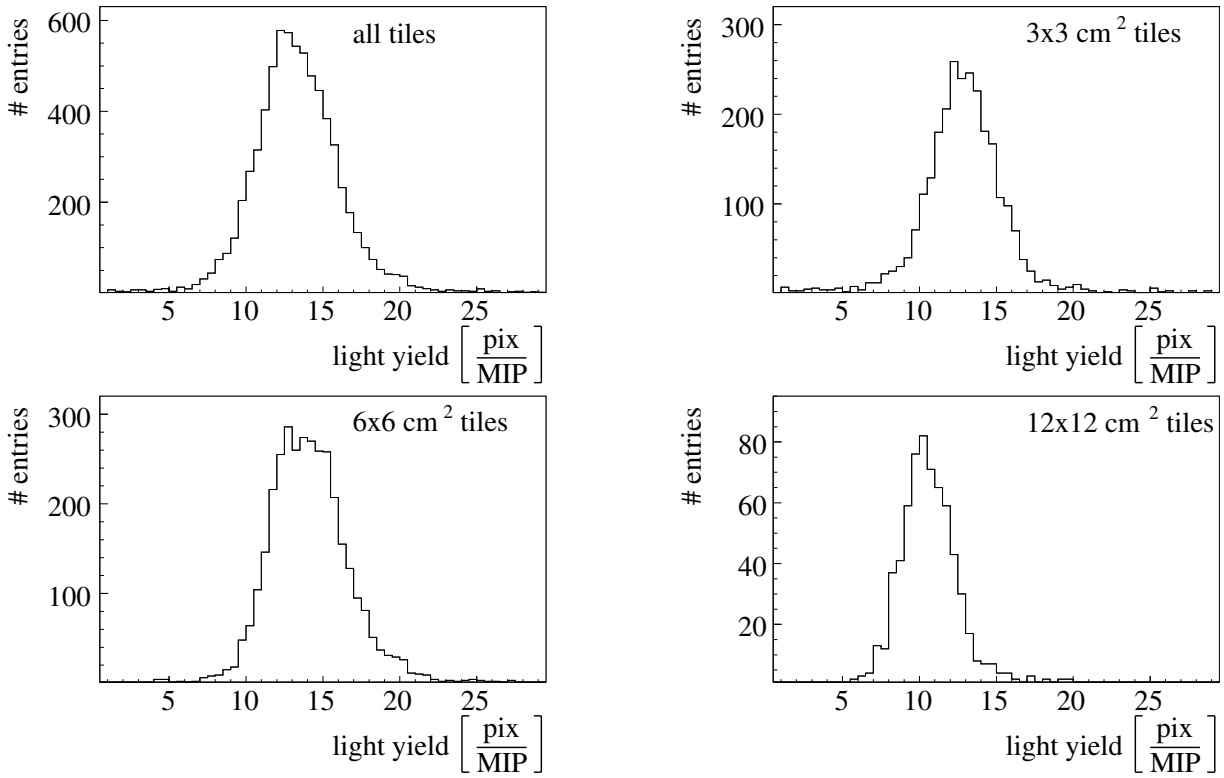

Figure 5.11: Lightyields of the AHCAL physics prototype cells measured after voltage adjustment. A muon beam is used as MIP source. Top left: All tiles (mean: 13.3 $\frac{\text{pix}}{\text{MIP}}$, spread: 2.9 $\frac{\text{pix}}{\text{MIP}}$). Top right: 3 x 3 cm^2 tiles (mean: 12.9 $\frac{\text{pix}}{\text{MIP}}$, spread: 2.9 $\frac{\text{pix}}{\text{MIP}}$). Bottom left: 6 x 6 cm^2 tiles (mean: 14.2 $\frac{\text{pix}}{\text{MIP}}$, spread: 2.7 $\frac{\text{pix}}{\text{MIP}}$). Bottom right: 12 x 12 cm^2 tiles (mean: 10.8 $\frac{\text{pix}}{\text{MIP}}$, spread: 2.4 $\frac{\text{pix}}{\text{MIP}}$).

Summary and Outlook

The physics prototype of a highly granular scintillator-steel sampling calorimeter with analogue readout for hadrons (AHCAL) built by the CALICE collaboration is the first large scale application for Silicon Photomultipliers (SiPMs), which are semiconductor-based photodetectors operated in Geiger mode. The sensitive layers of the prototype consist of a total of 7608 single plastic scintillator tiles. The scintillation light from each of these tiles is measured by an individual SiPM.

In this thesis, calibration data collected with the AHCAL physics prototype at DESY and during testbeam experiments at CERN and FNAL are used to investigate SiPM properties relevant for the calibration of the prototype. The effective number of pixels influences the non-linear response of the photodetectors. The temperature and voltage dependencies of the gain and the response of the SiPMs define the stability of any calibration procedure.

The effective number of pixels of the SiPM-tile systems used in the AHCAL physics prototype is $\approx 80\,\%$ smaller than determined by measurements performed on the bare SiPMs. This effect is attributed to a mismatch between the sensitive area of the SiPMs of $1\,\mathrm{mm}^2$ and the diameter of the wavelength-shifting fibres. The ratios allow for a rescaling of response curves measured on the bare SiPMs in a laboratory setup to describe the saturation behaviour of the mounted SiPMs inside the prototype.

The voltage and temperature dependencies of the gain and the response A^{MIP} to muons are quantified for more than $80\,\%$ of the SiPMs in the AHCAL physics prototype. The results from two independent measurements are consistent within $4\,\%$ for the voltage dependence of the gain, $12\,\%$ for the temperature dependence of the gain and $11\,\%$ for the voltage dependence of A^{MIP}. The temperature dependence of the breakdown voltage of the SiPMs is deduced with a precision of $14\,\%$. All relations, their systematic uncertainties and their spread within the studied SiPM sample are summarised in table 4.1. The results agree with previous measurements performed on the bare SiPMs within 2σ.

Successful applications of procedures to shift the calibration constants, i.e. the gain of the SiPMs and the MIP coefficient A^{MIP} of the cells, to different operation conditions are presented. The systematic uncertainties introduced by these procedures are established. Calculating the effects of voltage changes of some $100\,\mathrm{mV}$ or temperature changes of some K on the gain leads to a relative error of $1-2\,\%$ of the result, which is compatible with the precision of a gain measurement of $\approx 1\,\%$. The relative error of MIP coefficients A^{MIP} shifted by a few $100\,\mathrm{mV}$ or a few K is $\approx 3\,\%$, which is slightly larger than the precision

of $\approx 2\,\%$ of measurements of A^{MIP}. A summary of these methods and the systematic uncertainties that are introduced by their application is given in table 5.1. The next step is to use these procedures in data analysis to correct for the effects of temperature variations. In addition, voltage adjustments can be used to compensate the effects of temperature changes on G and A^{MIP} durig operation to stabilise the detector calibration.

An alternative method using gain measurements instead of temperature measurements to correct A^{MIP} for temperature changes is discussed. The uncertainties of the obtained relations between the MIP responses and the gains are large ($\approx 30\,\%$). If these uncertainties are reduced by further measurements, this correction method is expected to be more accurate than the correction using temperature measurements.

The light yield of the cells is a measure of the performance of the AHCAL physics prototype. According to studies performed during the construction of the prototype, this performance is optimal at a light yield of $15\,\frac{\text{pix}}{\text{MIP}}$. A procedure to scale the light yield via voltage adjustment is presented in this thesis. The application of this procedure during the detector commissioning at FNAL successfully shifts the mean light yield of the 6 x 6 cm^2 cells to $14.2\,\frac{\text{pix}}{\text{MIP}}$ with a spread of $2.7\,\frac{\text{pix}}{\text{MIP}}$. This matches the desired value of $14\,\frac{\text{pix}}{\text{MIP}}$, which is chosen instead of $15\,\frac{\text{pix}}{\text{MIP}}$ to keep the applied voltages smaller. Due to the light yield variations between the cells of different size, the achieved lightyields are only $12.9\,\frac{\text{pix}}{\text{MIP}}$ with a spread of $2.9\,\frac{\text{pix}}{\text{MIP}}$ for the 3 x 3 cm^2 cells and $10.8\,\frac{\text{pix}}{\text{MIP}}$ with a spread of $2.4\,\frac{\text{pix}}{\text{MIP}}$ for the 12 x 12 cm^2 cells. Applying voltage changes to individual SiPMs instead of averaging the adjustments over half-modules can reduce these discrepancies. For the AHCAL physics prototype, these individual adjustments are difficult to realise due to constraints of the used VFE electronics.

For the temperature sensors used in the calorimeter prototype, an improvement of the absolute calibration on the centigrade scale is achieved. In order to maintain a low calorimeter temperature and a flat temperature profile, cooling the CMBs and the VFE electronics is necessary. During the past test beam periods, this cooling was achieved by the use of fans. Since temperature shifts in the detector prototype do not occur for individual cells, but only for larger areas inside the detector, adequate averaging procedures could increase the precision of quantifying these collective drifts.

The investigation of the voltage and temperature dependencies of SiPM parameters done within this thesis shows that these relations vary by more than $10\,\%$ between the single SiPMs. Using individual values for each device yields good results. Whether the use of means instead of device-specific values degrades the precision of the correction or the adjustment procedures significantly still needs to be evaluated. The accuracy of the extracted dependencies is limited by the temperature stability and uncertainties of the temperature measurements within the AHCAL physics prototype. For future applications of SiPMs, all dependencies should be determined already during production in a laboratory setup under well-known conditions.

Bibliography

[1] E. Lohrmann, *Hochenergiephysik*, Teubner, 5th edition (2005), ISBN 3 519 43043 6.

[2] B. R. Martin and G. Shaw, *Particle Physics*, Wiley, 2nd edition (2006), ISBN 0 471 97285 1.

[3] J. Brau *et al.*, *International Linear Collider reference design report. 1: Executive summary. 2: Physics at the ILC. 3: Accelerator. 4: Detectors* (2007), ILC-REPORT-2007-001.

[4] T. Behnke, *The ILD starting point: GLD and LDC*, Presentation given at the ILD Workshop at DESY, Zeuthen, 14-16 January 2008.

[5] J. C. Brient, *Improving the jet reconstruction with the particle flow method: An introduction*, Prepared for 11th International Conference on Calorimetry in High-Energy Physics (Calor 2004), Perugia, Italy, 28 Mar - 2 Apr 2004.

[6] *Memorandum of Agreement between the members of the CALICE collaboration* (2005), http://polywww.in2p3.fr/flc/MOA.pdf.

[7] R. Wigmans, *Calorimetry*, Oxford University Press, 1st edition (2000), ISBN 0 19 850296 6.

[8] C. Amsler *et al.*, *The Review of Particle Physics*, Physics Letters **B667**(2008) 1, http://pdg.lbl.gov.

[9] P. Buzhan *et al.*, *An advanced study of silicon photomultiplier*, ICFA Instrum. Bull. **23**(2001) 28.

[10] P. Buzhan *et al.*, *Silicon photomultiplier and its possible applications*, Nucl. Instrum. Meth. **A504**(2003) 48.

[11] B. Dolgoshein *et al.*, *Status report on silicon photomultiplier development and its applications*, Nucl. Instrum. Meth. **A563**(2006) 368.

[12] *Hamamatsu photonics*, http://www.hamamatsu.com/index.html.

[13] M. Yokoyama *et al.*, *Development of multi-pixel photon counters* (2006), arXiv:physics/0605241v1.

[14] S. Gomi *et al.*, *Development and study of the multi pixel photon counter*, Nucl. Instrum. Meth. **A581**(2007) 427.

[15] H. Spieler, *Semiconductor Detector Systems*, Oxford University Press, 1st edition (2005), ISBN 0 19 852784 5.

[16] S. Uozumi, *Study of the MPPC performance*, Presentation given at the ILC Workshop in Valencia, 6-10 November 2006.

[17] S. Uozumi, *Study and development of multi pixel photon counter for the GLD calorimeter readout*, PoS **PD07**(2007) 022.

[18] W. R. Leo, *Techniques for Nuclear and Particle Physics Experiments*, Springer, 2nd edition (1994), ISBN 0 387 57280 5.

[19] M. Groll, *Construction and Commissioning of a Hadronic Test-Beam Calorimeter to Validate the Particle-Flow Concept at the ILC*, Ph.D. thesis, DESY (2007), DESY-THESIS-2007-018.

[20] A. Vargas, *Hcal operation and calibration at fnal*, Presentation given at the CALICE meeting in Manchester, 8 - 10 September 2008.

[21] N. Wattimena, *Commissioning of an LED Calibration & Monitoring System for the Prototype of a Hadronic Calorimeter*, Diploma thesis, DESY (2006), DESY-THESIS-2006-039.

[22] B. Lutz, *Commissioning of the Readout Electronics for the Prototypes of a Hadronic Calorimeter and a Tailcatcher and Muon Tracker*, Diploma thesis, DESY (2006), DESY-THESIS-2006-038.

[23] CALICE Collaboration, M. Danilov, *Scintillator tile hadron calorimeter with novel SiPM readout*, Nucl. Instrum. Meth. **A581**(2007) 451, 0704.3514v1.

[24] M. Reinecke, *HCAL Readout Boards - User Manual* (2005).

[25] N. D'Ascenzo, *The response of the HCAL to muons: results from the test beam*, Presentation given at the CALICE meeting at DESY, 12 - 14 February 2007.

[26] A. Vargas, *private communication.*

[27] S. Reiche, *Studies for the Optical Read-Out of a Hadronic Tile-Fibre-Calorimeter for TESLA*, Diploma thesis, University of Hamburg (2001).

[28] R. Brun *et al.*, *ROOT Data Analysis Framework*, http://root.cern.ch/.

[29] S. Richter, *Validation of the Calibration Procedure for a Highly Granular Calorimeter with Electro-Magnetic Processes*, Diploma thesis, DESY (2008), in preparation.

[30] A. Vargas, *MIP Calibration of the AHCAL*, Presentation given at the internal FLC meeting at DESY, 11 August 2008.

[31] National Semiconductor, *LM 35 Precision Centigrade Temperature Sensor* (1999), `http://www.national.com/mpf/LM/LM35.html`.

[32] ISEG, *8-channel High Voltage Power Supply EHQ 8605p 156F (Operators Manual)* (2004), `http://www.desy.de/~sven/Projects/HCAL/HV_Power/EHQ8405x_156V311eng.pdf`.

[33] R. J. Barlow, *Statistics*, Wiley, 1st edition (1989), ISBN 0 471 92295 1.

[34] V. Blobel and E. Lohrmann, *Statistische und numerische Methoden der Datenanalyse*, Teubner, 1st edition (1998), ISBN 3 519 03243 0.

[35] E. Garutti, *private communication.*

[36] N. Meyer, *private communication.*

[37] A. Kaplan, *private communication.*

List of Figures

List of Tables

Danksagung

Ich bedanke mich bei der gesamten Gruppe FLC für ihre Hilfsbereitschaft und für das stets angenehme Arbeitsklima. Mein besonderer Dank gilt Erika Garutti und Niels Meyer für die gute Betreuung, sowie Alexander Kaplan und Andrea Vargas für die gute Zusammenarbeit. Ich danke allen, die mir hilfreiche Hinweise zum Schreiben dieser Arbeit gegeben haben. Außerdem danke ich Johannes Haller für das Zweitgutachten.

Im Rahmen dieser Arbeit konnte ich an der Vorbereitung des AHCAL Prototypen für Testrahlmessungen am Fermilab und am Betrieb des Detektors vor Ort mitwirken. Ich bedanke mich für diese großartige Gelegenheit, und ich danke allen Beteiligten für ihre Unterstützung.

Erklärung

Hiermit versichere ich, die vorliegende Arbeit selbständig und nur unter Verwendung der angegebenen Quellen und Hilfsmittel verfasst zu haben. Ich gestatte die Veröffentlichung dieser Arbeit.

Nils Feege